Institut für Lufttransportsysteme

Hamburg University of Technology

MANTA

NASA DLR Aeronautical Design Challenge

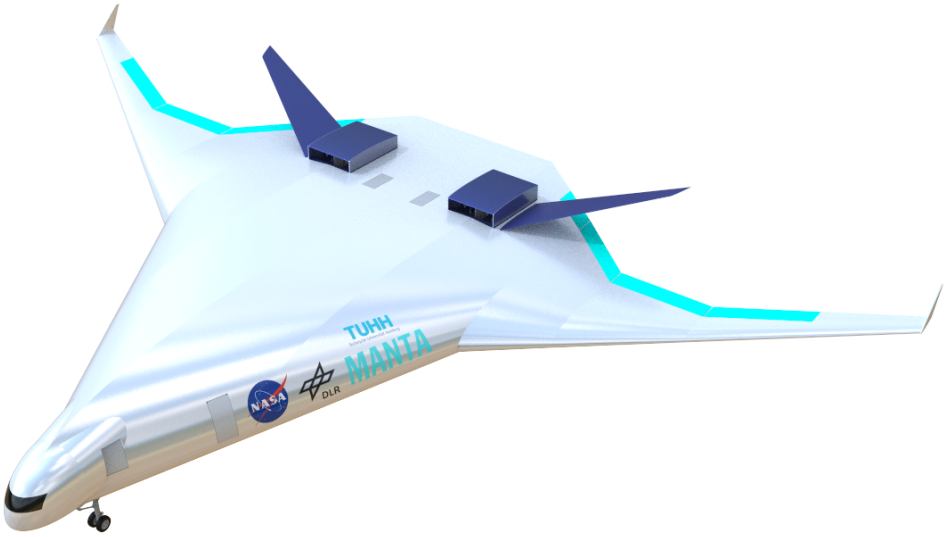

Team Members
Ahmet Akyüz, B.Sc.
Eduardo Zegarra Berodt, B.Sc.
Ghassen Hajiri, B.Sc.
Philip Salmang, B.Sc. (Team Leader)
Rhea Shah, B.Sc.
Xiaowei Zhu, B.Sc.

Academic supervision by
Prof. Dr.-Ing. Volker Gollnick

Submitted on July 18, 2021
Institute for Air Transport Systems
Hamburg University of Technology

Abstract

(EN) The NASA/DLR Design challenge poses students with the task to develop an efficient 150-seater aircraft using alternative fuel, hydrogen. This design report presents a possible solution to the challenge. The use of a combination of well-known design methods and the advantage of today's available software made it possible to evaluate and optimize an unconventional aircraft.

The resulting design is a blended-wing-body aircraft capable of providing the passengers with a safe and comfortable cabin interior, propelled by electrical motors powered by a hydrogen fuel cell. The hydrogen is stored in liquid form in thermally isolated tanks to keep with the extremely low temperature requirements. The environmental goals set for the aircraft are achieved by eliminating and reducing the generation of CO_2 and NO_x gases, hence reducing the climate impact of the flight.

The design sets a precedent for the future of aviation with a 2035 horizon. The big step forward into green technologies should also be met with a radical change of what a conventional aircraft is supposed to be. The blended wing makes it directly apparent that the new era of commercial travel is upon us.

(DE) Die NASA/DLR Design Challenge stellt Studenten vor die Aufgabe ein effizientes 150-sitziges Flugzeug zu entwickeln, dass mit dem alternativen Kraftstoff Wasserstoff betrieben wird. Dieser Projektbericht stellt eine mögliche Lösung für die Herausforderung vor. Durch die Verwendung einer Kombination aus bekannten Entwurfsmethoden und dem Vorteil der heute verfügbaren Software war es möglich, ein unkonventionelles Flugzeug zu evaluieren und zu optimieren.

Der resultierende Entwurf ist ein Blended-Wing-Body Flugzeug, dass den Passagieren einen sicheren und komfortablen Innenraum bietet und von Elektromotoren angetrieben wird. Diese werden von einer Wasserstoff-Brennstoffzelle versorgt. Der Wasserstoff wird in flüssiger Form in thermisch isolierten Tanks gespeichert, um die erforderlichen extrem niedrigen Temperaturen einzuhalten. Die für das Flugzeug gesetzten Umweltziele werden durch die Vermeidung und Reduzierung der Erzeugung von CO_2 und NO_x Gasen erreicht, wodurch die Klimabelastung im Flug reduziert wird.

Das Design setzt einen Präzedenzfall für die Zukunft der Luftfahrt mit einem Zeithorizont von 2035. Der große Schritt in Richtung grüne Technologien sollte auch mit der radikalen Veränderung dessen einhergehen, was ein konventionelles Flugzeug sein soll. Der Blended Wing macht direkt deutlich, dass die neue Ära des kommerziellen Reisens angebrochen ist.

Team Members

Ahmet Akyüz, B.Sc.
Power Generation & Emissions

Eduardo Zegarra Berodt, B.Sc.
3^{rd} Semester M.Sc. Aircraft Systems Engineering

Initial Sizing, CAD Design & Propulsion

Ghassen Hajiri, B.Sc.
2^{nd} Semester M.Sc. Aircraft Systems Engineering

Range Analysis, V-n Diagram & Engine Selection

Philip Salmang, B.Sc.
3^{rd} Semester M.Sc. Aircraft Systems Engineering

Project Management & Aerodynamics

Rhea Shah, B.Sc.
2^{nd} Semester M.Sc. Aircraft Systems Engineering

FEM Analysis, Costs & Sustainability

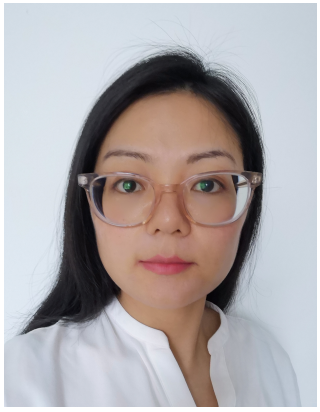

Xiaowei Zhu, B.Sc.
9^{th} Semester B.Sc. Mechanical Engineering

Cabin & Image Render

TUHH
Technische Universität Hamburg

ILT
Institut für
Lufttransportsysteme

TUHH, Institut für Lufttransportsysteme, D-21079 Hamburg

Institut für Lufttransportsysteme
Prof. Dr.-Ing. Volker Gollnick
Blohmstr.20
D-21079 Hamburg

Datum und Zeichen Ihres Schreibens	Geschäftszeichen	Hamburg,
	Prof. Dr.-Ing. Volker Gollnick	16. Juli 2021

Bescheinigung und Freigabe des Beitrags zur DLR/NASA-Design-Challenge 2021

Hiermit wird bescheinigt, daß der Beitrag der Studierenden zum Studierendenwettbewerb DLR-NASA-Design Challenge 2021 am Institut für Lufttransportsysteme geprüft und freigegeben wurde. Die Einreichung des Beitrags wird hiermit befürwortet. Ferner wird hiermit die eigenständige Anfertigung der Arbeit durch die Studierenden bestätigt.

Für weitere Rückfragen stehen Herr Jens Thöben, M.Sc. jens.thoeben@tuhh.de sowie Herr Jan Tomalka, M.Sc. jan.tomalka@tuhh.de oder ich gerne zur Verfügung.

Mit freundlichen Grüßen

Volker Gollnick
Institutsleiter

Postanschrift
21071 Hamburg

Besucheranschrift
Blohmstraße 20
21079 Hamburg

Telefon
+49 (0) 40 428 78-4196

Fax
+49 (0) 40 428 78-2979
www.tu-harburg.de/ilt

E-Mail
volker.gollnick@tu-harburg.de

Table of Contents

List of Figures

List of Tables

Nomenclature

List of Acronyms

LH_2	Liquid hydrogen
LOX	Liquid oxygen
AD	Arbeitsgemeinschaft Druckgeräte
Al	Aluminium
AoA	Angle of Attack
APU	Auxiliary power unit
ATA	Air Transport Association
ATC	Air Traffic Control
BC	Business Class
BF	Block Fuel
BFL	Balanced Field Length
bhp	Brake horse power
BWB	Blended Wing Body
CAD	Computer Aided Design
CFD	Computational Fluid Dynamics
CFRP	Carbon Fiber Reinforced Plastic
CoG	Center of Gravity
Cr	Chromium
CVR	Cockpit Voice Recorder
DAPCA	Development and Procurement Costs of Aircraft Model
DLR	German Aerospace Center
DOC	Direct Operating Cost
E-motor	Electric Motor
ECS	Environmental Control System
EIS	Entry into service
ELT	Emergency locator transmitter
FDR	Flight Data Recorder
ICAO	International Civil Aviation Organization
IOC	Indirect Operating Cost
ISA	International Standard Atmosphere
LCC	Life Cycle Cost
MH	Martin Hepperle
MSL	Mean sea level
MTOW	Maximum Take-off Weight
NASA	National Aeronautics and Space Administration
Ni	Nickel
NTU	Number of transfer units
ODA	Oxygen depleted layer
OEI	One Engine Inoperative
OER	Oxygen Excess ratio
OLED	Organic Light-Emitting Diodes

OME	Operational Mass Empty
Opp	Operators Items
PAX	Passenger
PEMFC	Proton-exchange membrane fuel cell
PGW	Propyl-glycol water solution
PL	Payload
RCF	Recycled Carbon Fiber
SAF	Sustainable Aircraft fuel
SI	International System
SOFC	Solid oxide fuel cell
TLAR	Top Level Aircraft Requirement
TUHH	Hamburg University of Technology
YC	Economy Class

List of Symbols

Symbol	Unit	Description
α	[°]	Angle of Attack
η	[%]	Efficiency
λ	[W/mK]	Heat Conductivity
λ	[-]	Oxygen Excess ratio
ρ	[kg/m³]	Density
ε	[%]	NTU ratio
ϑ	[°C]	Temperature
A	[m²]	Area
a	[m/s]	Speed of Sound
C	[J/K]	Heat Capacity
C_L	[-]	Lift Coefficient
C_M	[-]	Moment Coefficient
c_P	[-]	Pressure Coefficient
D	[m]	Diameter
E	[J]	Energy
E	[Pa]	Saturation pressure
e	[C]	Elementary charge
I	[A]	Electric Current
M	[kg/mol]	Molar Mass
m	[kg]	Mass
Ma	[-]	Mach number
n	[-]	Quantity
n	[1/s]	Revolution
n	[-]	polytropic Exponent
P	[W]	Power
p	[Pa]	Pressure
Re	[-]	Reynolds Number
T	[K]	Temperature
T	[N]	Thrust
t	[s]	Time
t	[m]	Thickness
V	[m³]	Volume
v	[m/s]	Velocity
W	[N]	Weight
x_{CoG}	[m]	Distance Radome CoG
x_N	[m]	Distance Radome Neutral Point

1. Market Analysis until 2035

The following chapter aims to explain the upcoming global trend of the aviation industry and from there derive the first step of the design process for the future aircraft concept.
Over the past decades, the aviation market has proven to be a steady growing market with an average annual growth rate of 4.3% and being nearly resilient to external shocks. Following a crisis, the aviation market tends to recuperate entirely resulting in nearly 9 million Revenue Passenger Kilometers (RPKs) in 2018 [Air17]. While the European and the North American markets have stagnated in growth, the emerging Central Asian market, being one of the strongest growing markets, will considerably form the future of Top Level Aircraft Requirements (TLARs). Until 2035, nearly 41% of the global aircraft demand will originate from the Central Asian market due to the strong correlation between revenue passenger kilometre (RPK) and gross domestic product (GDP). Additionally, a significant shift of demand to single-aisle aircraft is seen. Nearly 70% of new deliveries until 2035 will be single-aisle aircraft, while large wide-body aircraft will only make up 1% [Boe16].
Presently, the goal of the aircraft design process is to reduce operating costs on standard design missions while meeting specific TLARs and meeting additional design limitations. The aim of being sustainable was not of high priority [Lin+20]. Nevertheless, the meaning of sustainable aviation becomes of greater importance, especially after CO_2 emissions surpassed 400 ppm for the first time in history in 2013. This rise of CO_2 emission in the atmosphere shows an undeniable relationship with the amount of fossil fuels that have been burned [Bar+87]. This can also be seen in figure 1.1.

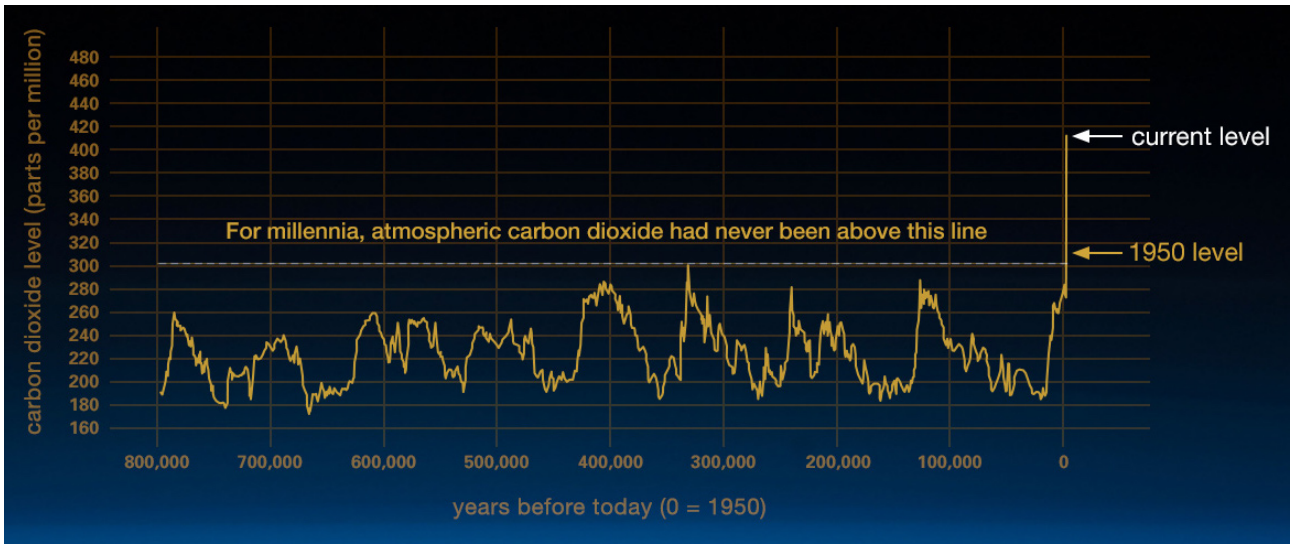

Figure 1.1.: Carbon Dioxide Levels [Cli]

Unfortunately, possible future revenue is the largest driver for future aircraft designs. It would be necessary to implement further restrictions on airlines in order to influence the possibility of a sustainable and environmental friendly future. In order to assess the behaviour, it is essential to consider the various factors that influence its framework conditions, like political and legal basics and fuel availability. Two impelling forces that will affect to future of sustainable aviation is the increase awareness of pollutants and global warming and the Paris Agreement from 2015 [Gre+21]. The Covid-19 pandemic has also been a major driver for the increasing awareness due to a rapid decrease of carbon emmission by a factor 2 to 3 during the global travel surge [Niž20]. As a consequence, the ultimate solution approach would be a non-polluting fuel produced from renewable sources. In addition to low emissions, hydrogen offers the great advantage of a three times higher energy density, compared to kerosene. Nevertheless, due to the very low volumetric energy density it requires the necessary provision of additional volume to accommodate the fuel [HHS06]. Consequently, there are some challenges, which have to be addressed, in order to establish a sustainable, efficient and competitive configuration. These challenges are focused on an overall efficient design of the aircraft and an often underestimated need for infrastructure. With this in mind, the design approach for a hydrogen-powered aircraft servicing multiple short-haul routes a day is driven towards fulfilling market demands while optimizing the synergy effects provided by the future hydrogen concept.

2. Methodological Analysis

In order to design the aircraft of tomorrow, current engineers can not hold on to the conventional designs of the past. Therefore, a Morphological Box (Section 2.1) and comprehensive Design Studies (Section 2.2) are conducted to enhance creativity and support a thinking-outside-the box mentality of all involved students on this project. Through this process, a suitable initial design is selected in section 2.2

2.1. Morphological Box

Based on current and future design and technological advances, a broad spectrum of different strategies can be identified on how to approach a new aircraft design. A Morphological Box is used to visualize possible design solutions and to point out the main options of how to proceed and what the initial design will look like. The Morphological Box is shown in figure 2.1. The indicated words show each solution for the desired parameter. However, not all solutions are implemented into the final design. Some solutions like the windowless cabin are not only a structural and design challenge, but also a challenge for the acceptance by the passengers on board. The aim is to use a video screen inside of a cabin resembling a window to produce the illusion of looking outside. Both the reasoning behind each parameter and the final design are explained later in this paper.

MORPHOLOGICAL BOX

Parameters	**Solutions**				
Energy Generation	Combustion	Fuel Cell	Backup Li-BAT	Fuel Cell and Combustion	
Placement Fuel tanks	Wing	Fuselage	Wing and Fuselage		
Configuration	Conventional	BWB	Hybrid Flying Wing	Struct Braced Wing	Box joined wing
Thrust Generation	Turbofan	Turboprop	Prop (Pure Electric)	Open Rotor	
Cabin	High-Tech	Windowless	With Windows	Regular Seats	Beds
Layout	Conventional	Double Bubble	Square	Ellipsoid	
Gear	Conventional	Gearless			
Materials	Alu	GLARE	GFRP		
Empennage	Traditional	only Vertical Stabilizer	V	None	
Emergency Energy	APU	RAT	BAT		
Highlight	Cabin	Superconductor			

Figure 2.1.: Morphological Box

2.2. Design Studies

The first step in every design process is to take a closer look at the set of requirements. In this case, the requirements are established by the two project partners, namely DLR and NASA [DLR21]. Global requirements begin with the mission definition as shown in table 2.1. The development focuses on a hydrogen-powered short- to medium-range civil aircraft design for at least 150 passengers (PAX) on a range farther than 2000 km (1080 nautical miles). Flight altitude is 3000 m (9843 ft) and higher, with a cruise Mach number of 0.7. For slow approaches, a speed of less than 130 knots is considered to be optimal. The effects on the atmosphere and an overall energy analysis should be taken into account. With more than 150 seats, the aircraft is considered a medium-size aircraft in commercial transport operations. This size of aircraft is normally used on short-/medium-range, regional routes. First marketing research on the existing fleet of aircraft with approximate 150 PAX is conducted. Table 2.2 shows the existing relationship between aircraft size (number of PAX) and design range. It shows most of the potential competitors to the new design of conventional configuration. To improve the conventional wing-cylindrical-fuselage-tail configuration of civil aircraft there are some popular ideas such as installing next-generation engines, using laminar flow, new airfoils and winglets to improve aerodynamics. Lightweight structure design is also an effective way to increase energy efficiency and reduce fuel consumption and more innovative systems such as more electric system architecture, active and adaptive control should be developed. However, the conventional Layout is gradually reaching an asymptotic limit in terms of efficiency,

especially from an airframe point of view [KS15]. So the 'new look' aircraft should be also considered for a green future. Four design options like nonplanar wings, the oblique flying wing, wings with a very high-aspect-ratio and flying wings are to be considered for unconventional configuration. Considering the large size of the hydrogen fuel tank and the possibility of better aerodynamic characteristics, it is decided to choose the concept of blended wing body (BWB) for the MANTA. The term BWB is used very often to account for configurations that may deviate from the pure flying wing shape to accommodate the payload. With blended wing bodies, the lift is produced both by the central body and by lateral wings. This contributes to a much better L/D ratio compared to the classical configuration.

Table 2.1.: NASA/DLR Aeronautics Design Challenge 2021 specifications [DLR21]

Constraint	Value/Description
Number of passengers	150
Passenger weight	80 $^{kg}/_{PAX}$ + 25 $^{kg}/_{PAX}$ Baggage
Crew	80 kg (flight deck and cabin)
Entry into service (EIS)	2035
Fuel	H_2/LH_2
Cruise speed	Ma = 0.7
Approach speed	$\leq$ 130 kts
Take-off field length (TOFL)	$\leq$ 2000 m
Range	$\geq$ 2000 km
Diversion range	200 NM
Altitude	$\geq$ 3000 m
Mission 1	Optimised for lowest climate impact
Mission 2	Optimised for lowest climate impact and maximum cost-effectiveness

Table 2.2.: Study of similar Aircraft Marketing

Aircraft type	Number of PAX	Range (km)
Required	150	$\geq$ 2000
A319neo	140	6850
A320neo	165	6300
B737 MAX 8	189	6704
B727-200	145	4020
C919	156	5555
DC-8-55	189	8700
DC-8-62	189	9600
Irkut MC-21-300	163	5900
DZYNE Ascent1600	165	6482

3. Blended Wing Body

3.1. Initial Sizing

The decision of a Blended Wing Body bears difficulties for the initial sizing of the aircraft. Since there are many unknown parameters, the initial sizing was based on the fixed design parameters like the payload and the fuel cell decided in figure 2.1. The aircraft is built around the cabin which has a fixed number of passengers and the hydrogen tanks sized according to the required volume. The cabin layout was configured early in the design process. More on the design of the cabin layout and its elements are discussed later in section 3.2. The determining parameters for the initial sizing were the length and diameter, as well as the required cabin height. Once the design for the cabin layout is set, divided into two classes, the next step determines the required volume for the liquid hydrogen tanks. Taking a 150 passengers aircraft with an energy requirement of 22 MW obtained from [Fel16] as a baseline, an initial value for the required tank volume is calculated to be around $80\,m^3$, which is divided into 4 equally sized tanks. This value would evolve as the specific requirements for the mission are more clearly examined during the iterative design of the MANTA.

3.1.1. Wing Design

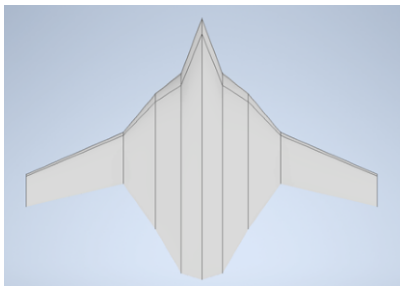

Figure 3.1.: First Iteration BWB Design

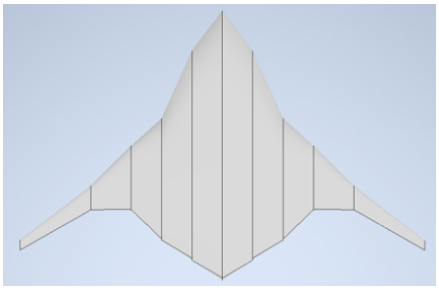

Figure 3.2.: Second Iteration BWB Design

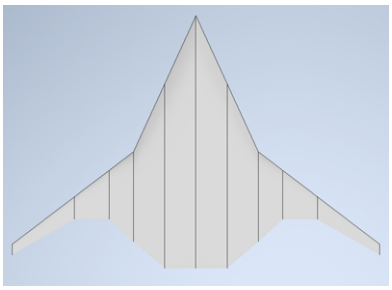

Figure 3.3.: Final Iteration BWB Design

For the design of the BWB many airfoils were considered. However, ultimately, the airfoil MH-91 [Hep21b] with a thickness of 14.98 % is chosen for the sections D and E, and the airfoil MH61 [Hep21a] with a thickness of 10.2 % for sections A through C as seen on figure 3.4. The MH-91 airfoil is able to conceal a large internal volume with a relatively short chord length, and is therefore suitable for the cabin section of the BWB. For the first iteration, the only objective is to conceal the structure of the cabin and the tanks with the airfoil as seen in figure 3.1, in order to get a better understanding of the dimensions of the aircraft. The structures are concealed within the airfoil but the proportions between the airfoils and the sweep angles required further optimization. The relationships found on [DJ19, pp.6-7] are used to optimize the sweep angle of the wing and the correlation between the different sections, thus the second iteration is developed as seen in figure 3.2. A final approach is performed to streamline the sweep angles of the wing and the center body, as well as to shorten the center airfoils chord length to reduce unused space. For the final design, the sweep angle is streamlined to 75° for the center body and 43° for the wing, as supported by [SQ06]. The final design is shown in figure 3.3. This design is then analyzed to obtain the aerodynamic properties as seen in section 3.3. The geometric parameters of the wing are summarized in table 3.1.

Table 3.1.: Wing Geometric Parameters

Parameter	Value	Description
S_{ref}	$619.35\,m^2$	Wing Area
AR	4.53	Aspect Ratio
b	53 m	Wing Span

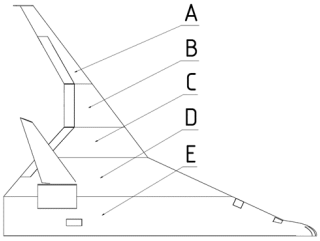

Figure 3.4.: Sections BWB

3.1.2. Mass Calculation

The mass for MANTA is calculated using a statistical mass approximation for the different systems and components of the aircraft. The equations used for the calculations are described in the *Luftfahrttechnisches Handbuch* (LTH) [DG11]. Since the LTH does not account for a BWB design, the blended wing was divided in sections as seen on figure 3.4, in order to calculate the mass. Sections A through C where calculated as a traditional wing and sections D and E as fuselage. To obtain the mass estimation of the fuselage, systems, furniture, and operational items, the length and diameter of the cabin as obtained from table A.1 and A.2, as well as the number of passengers are required. Table 3.2 shows the cabin mass approximation for 150 passengers.

The masses of the wings, propulsion system (props, E-Motor, inverter/controller), landing gear, and energy system are obtained after many iterations and optimization steps. Initial approximations and assumptions are taken from literature. To calculate the wing's mass, the equations found in the LTH [DG11] are applicable once the wing geometry is determined. For the landing gear, the weight is calculated from the maximum landing weight, which is obtained by subtracting the mass of the block fuel (BF) from the maximum take-off mass (MTOM). The required energy consumption is analyzed in section 3.4 as it is a decisive factor for the propulsion system and the power generation systems.

The mass calculation for the power generation system is detailed in chapter 4. Once the required thrust and mechanical power needed for the different flight phases is determined in subsection 3.4.2, a propulsion system that can satisfy the different flight phases was selected. The NASA N3-X electric fan propulsion system [FB09] is selected for the MANTA and downscaled to satisfy the requirements. More on the propulsion system is found in section 3.5. From the flight performance analysis in section 3.3, it was determined that two horizontal stabilizers are needed for MANTA, the weight of which is also calculated using the LTH [DG11] method. The results for the iterative mass systems can be found in table 3.3. The final mass calculation are summarized in table 3.4. The mass of the block fuel for a 2000 km mission with a 200 NM loiter is used for calculating the maximum take-off mass.

Table 3.2.: Mass Cabin

Parameter	Value
Fuselage	8193 kg
Systems	4218 kg
Opp (Short Range)	5963 kg
Furniture	2095 kg

Table 3.3.: Mass Iterations

Parameter	Value
Wing	13 735 kg
Vertical stabilizers	1012 kg
Landing gear	3322 kg
Propulsion systems	4218 kg
Energy system empty	20 796 kg

Table 3.4.: Mass MANTA

Parameter	Value
OME	63 150 kg
m_{PL}	15 750 kg
m_{BF}	1276 kg
MTOM	80 176 kg

The mass range diagram, as seen in figure 3.5, is calculated by using the Breguet range equation for a constant cruise speed [Gud13]. For an approximation of the fuel consumption per hour $\mathrm{W_{fuel/h}}$ the maximum block fuel m_{BF}, taken from table 3.4, is divided by the total flight time 3.3 h as seen in table 3.7. To obtain the specific fuel consumption (SFC) c_t in $\frac{\mathrm{kg\,h}}{\mathrm{N}}$ (Equation 3.1) according to [Gud13], $W_{\mathrm{fuel/h}}$ is divided by the thrust during cruise T_{cruise} as seen in equation 3.4. This yields a SFC of $c_t = 0.0132\ \frac{\mathrm{kg\,h}}{\mathrm{N}}$.

$$c_t = \frac{(W_{\mathrm{fuel/h}})}{T_{\mathrm{cruise}}} \tag{3.1}$$

Two segments are analyzed for the mass range diagram. The first for the maximum take-off mass with maximum payload, equal to 2637.7 km. The second range is considered for a take off mass without PL, which is equal to the OME plus the BF equal to 3289.1 km.

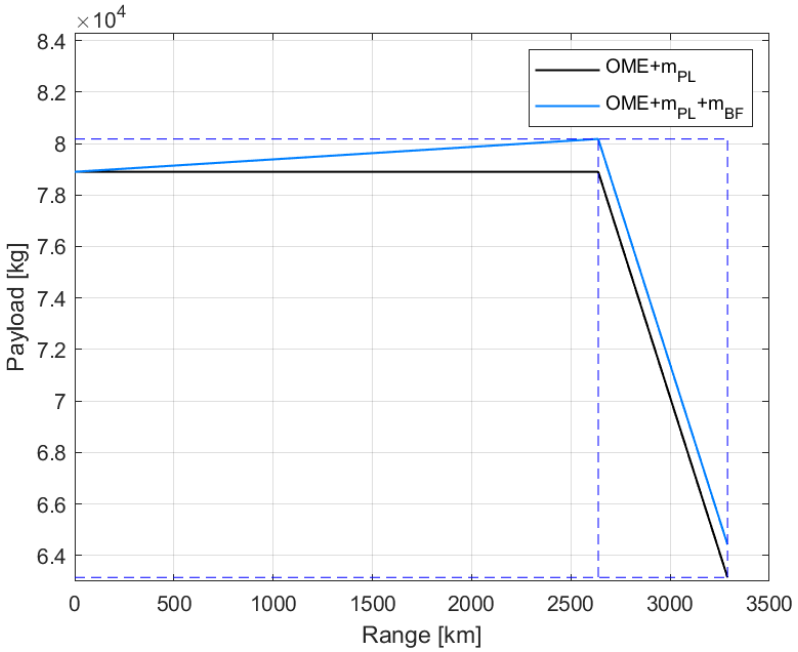

Figure 3.5.: Payload Range Diagram

3.2. Cabin Configuration

According to [KS15] the major challenges of BWB are numerous and related to the cabin, like evacuation scenarios, passenger comfort, and passenger acceptance. Thus during the cabin design, three perspectives: passenger, airlines, and climate are considered. From the passenger's perspective safety, comfort, and acceptance of virtual windows is taken into account. From the airline's side, the economic aspects are given top priority.

3.2.1. Key Conditions

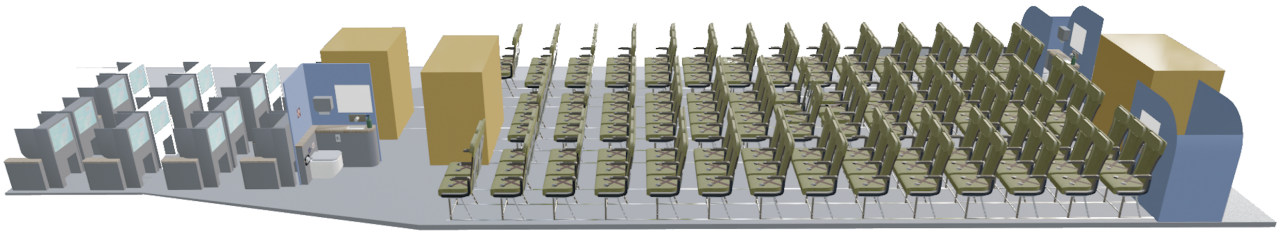

Figure 3.6.: Full Cabin Side View

The total cabin length is 22.35 m with a two-class arrangement for a total of 150 passengers (see Figure 3.6). The cabin is divided into a business class (BC)/economy class (YC) splitting of 16/134 and it's cross-section is shown in figure 3.8. A wide BWB fuselage configuration is applied, aiming at the beneficial aerodynamic features and space for the liquid hydrogen tank. Aircrafts having only one passenger aisle, no more than 3 seats abreast may be placed on each side of the aisle in any row [Age20]. Therefore, a 3-4-3 abreast configuration is chosen fulfilling the airworthiness requirements from CS 25.817.

Two 'Type I' and one 'Type III' emergency exits on each side allow a quick evacuation of the passengers in case of emergency. The passenger evacuation is discussed in section 3.2.2. The cargo compartment is located in the underfloor of the EC-class passenger cabin. For 150 Passenger 4 LD3 containers are needed.

They offer a load capacity of 36 m^3. More detailed dimensions of cabin interior are shown in table A.1 and table A.2. Considering the difficulty of external windows for a BWB they are replaced with virtual windows (see figure 3.7). The virtual windows are made using organic light-emitting diodes (OLEDs), a combination of advanced materials that emit their own light when activated by electricity. The screens are of a similar size as of a B787 conventional window. Regarding the size, smaller screens are better suited, as larger displays produce optical pollution causing passenger visual fatigue. Unlike LED and plasma displays, they do not need backlighting, allowing them to use less energy and to be much thinner than other displays and traditional windows. Since 2017 Emirates' Boeing 777-300ERs is the first aircraft that offers the first-class suites along the center of the plane with virtual windows. This new technology received good feedback from passengers. By replacing the traditional windows, the aircraft becomes lighter, can fly faster, burns less fuel, and flies higher. To avoid claustrophobic sensations, the virtual windows can display what is going on outside in real-time with externally mounted fiber-optic cameras.

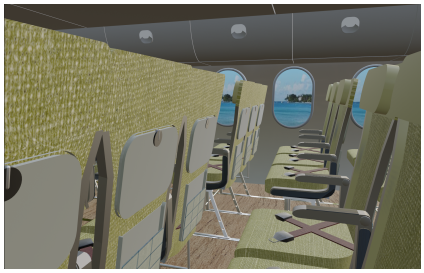

Figure 3.7.: Cabin With Virtual Window

According to Kozek, M. et al [JM13], colored lighting influences psychological and physiological well-being. In order to reduce passenger discomfort with a windowless cabin, a colored LED lighting system is used in the MANTA interior design. Yellow can be beneficial in making passengers more relaxed. Besides, yellow and blue hues are useful for increasing and decreasing temperature sensation respectively which could further result in a reduction of environmental control system (ECS) performance and energy consumption. In comparison to incandescent lighting, LED lighting has reduced power consumption and a longer operating lifetime.

Carbon fiber-reinforced composites are popular materials in aircraft manufacturing in recent years because of their durability, lightweight and ability to be formed in complex shapes. More than half of the structure of an A350 XWB is composite. One particular standout material is carbon-fiber-reinforced plastic (CFRP) as it is lighter than aluminum, stronger than steel, and more resistant against corrosion. According to [Pim11], from 2015 to 2035 the composite demand in aerospace will be doubled and carbon fiber waste from only production scrap will be up to 75 000 tons. Nowadays, more and more firms and institutes pursue composites recycling. The energy consumed in recycling methods ranges from 2 to 10 [kWh/kg] and is far below the energy consumed to manufacture the virgin carbon fiber (55–165 [kWh/kg]) [Hon15]. Therefore, from the aspect of energy consumption, the recycling method is economical, and hence recycled carbon fiber (RCF) materials would be used in our cabin interior sidewall panel. Additionally, beyond its potential to reduce molding time and cost in post-finishing, the RCF sidewalls also achieved a 22% weight reduction. The dimpling effect is also reduced, which often appears in conventional sidewall production in the laminate bridges of the honeycomb cells. [Gar16].

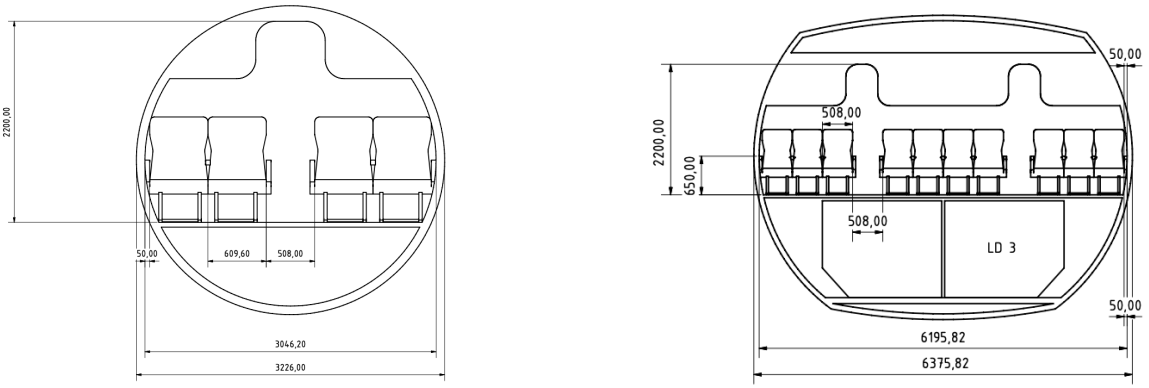

(a) BC Cross Section

(b) YC Cross Section

Figure 3.8.: Cabin Cross Section

3.2.2. Emergency Evacuation Simulation

The certification regulations for airworthiness state that the time to evacuate a civil aircraft, in case of an emergency, must be less than 90 seconds with half of all exit doors closed [Age20].

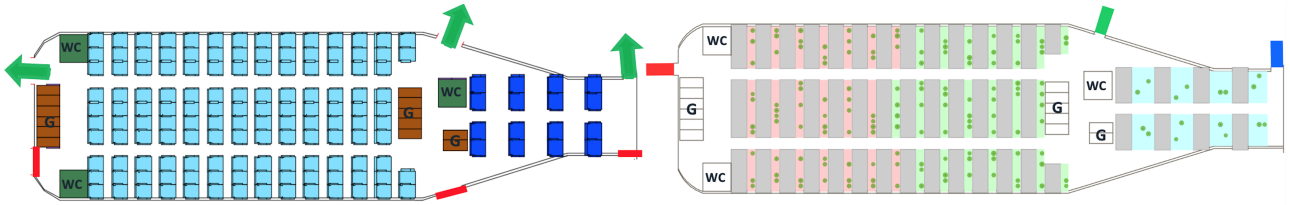

(a) Half of Exit Doors are Closed (b) Modeled Cabin and PAX in Evacuation Simulation

Figure 3.9.: Cabin Evacuation Simulation

The software *crowd:it* by *Accu:rate* is used to simulate the cabin emergency evacuation [acc11]. The inputs for the simulation are the cabin layout (cabin width, cabin length, exits, seat abreast, seat pitch, lavatories, and galleys), passenger setting, and passenger behavior setting. The initial state for the simulation is shown in figure 3.9 with the doors on the right side of the aircraft closed. A total of 150 passengers are generated within the first second. Each has a different response time ranging between zero and ten seconds. The value of "comfort distance" represents the human behavior during the evacuation situation and corresponds to a dense crowd. In this case, the distance is set to 0.7 m for passenger, according to [AB20]. This value is regarded as the average arm length of an European adult. The size of doors is reduced in the simulator so that only one passenger will be allowed to exit at a time. 66 passengers go through the Exit 1 (Door type I: 0.508 m x 1.85 m), 68 passengers go through the Exit 2 (same size as Exit 1) and 16 passengers go through the Exit 3 (Door type III: 0.508 m x 1.2 m). The speed of a passenger depends on the passenger's gender, age and passenger load (see Table B.3 , Table B.4 and Table B.5). The figure 3.10 displays the number of passengers inside MANTA over the evacuation time with half of all exit doors closed. The result for the evacuation time is 32 seconds. It fulfills the safety requirements.

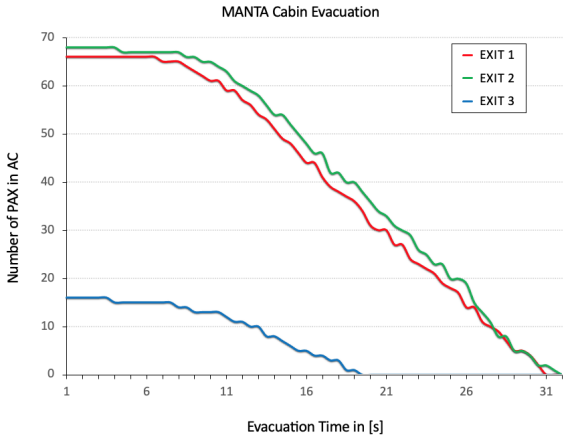

Figure 3.10.: Number of PAX inside MANTA

3.3. Flight Performance

The following chapter aims to describe the aerodynamic characteristics of MANTA. After the CFD method is explained, a thorough Gust-Load Analysis is performed in the subsequent section.

3.3.1. Aerodynamic Characteristics

Due to the selection of a Blended Wing Body and the absence of wind tunnel testing, computational fluid dynamics are used for the aerodynamic analysis. The open-source tool OpenVSP [Lan21] is used. The analysis is carried out with the low fidelity vortex lattice method. 2^{nd} Karman–Tsien compressibility correction is used to extend the solutions to compressible subsonic flows. A thorough design of the wing is already described in subsection 3.1.1. The aerodynamics analysis quickly shows that a widespread area in the aft of the fuselage contributes only marginally to the lift. At higher angles of attack, $\alpha > 20°$, the airflow separation and a positive pressure distribution become evidently visible (Figure 3.11 (b)). This distribution is visible up to the outboard ailerons. As a comparison, the pressure distribution of an AoA of $\alpha = 3°$ is shown in figure 3.11 (a).

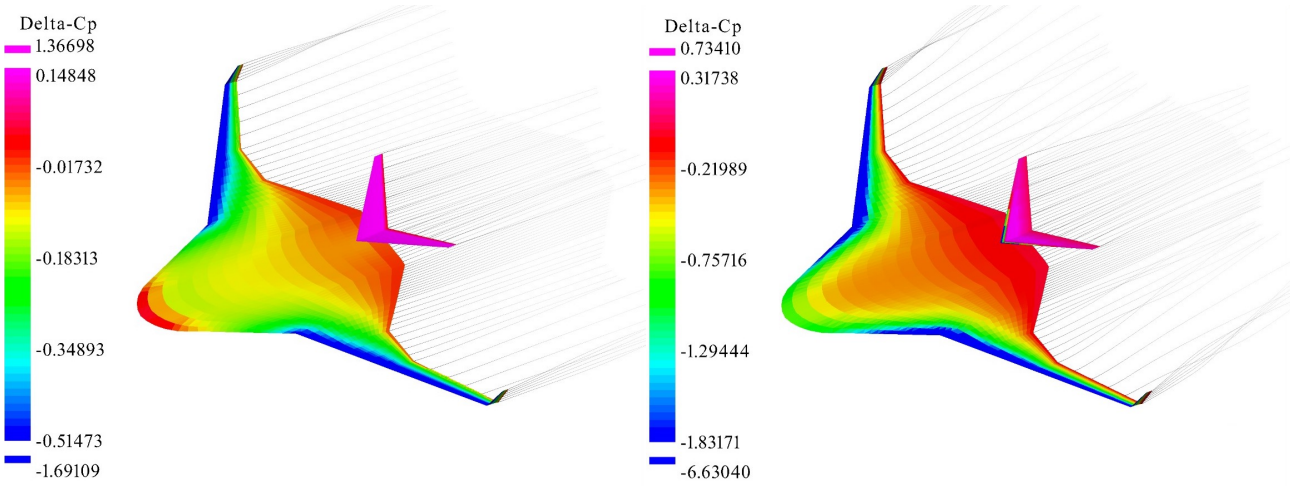

(a) 3° AoA (b) 20° AoA

Figure 3.11.: Pressure distribution

Even though the fuselage still generates enough lift beyond this angle of attack to fly horizontally, the outer part of the wing has insufficient airflow over the control surfaces. This can result in lateral instability if the AoA is increased any further. This instability is very crucial during the phases of take-off and landing since high angles of attack are used to generate sufficient lift during these slow phases of flight. The small margin of recovery due to the proximity to the ground can be fatal. Therefore, MANTA is limited to a 20° angle of attack using angle of attack limiters [OM14]. Similar to a conventional aircraft, the amount of drag on the outer part of the wing is minimized using higher aspect ratio wings. Due to the early separation of airflow along the main fuselage, the chord length was shortened by almost 6 m resulting in a significant weight reduction. The relatively short cabin length results in minor Center of Gravity (CoG) variations and low pitch inertia. This, combined with moderate wing loading, lowers control power requirements. The CoG is also an important input for the longitudinal stability of the BWB. To meet the stability requirements and achieve an elliptical lift distribution to reduce induced drag, modifications to the angle of incidence of certain wing portions are applied. The angles are varied from 0° up to 4°. Figure 3.12 shows that the load distribution is close to elliptic. The following two requirements must be met to achieve a stationary, stable, and trimmed flight condition. First, the pitching moment must equal zero (Equation 3.2). Second, the center of gravity is positioned in front of the neutral point of the aircraft, resulting in a negative gradient of the moment coefficient polar (Equation 3.3). As a result, at zero lift, the moment coefficient must be greater than zero [RWH14].

$$\frac{\partial C_M}{\partial C_A} = \frac{\partial C_M}{\partial \alpha} = \frac{C_{M\alpha}}{C_{A\alpha}} \tag{3.2}$$

$$\frac{\partial C_M}{\partial C_A} = -\frac{x_N - x_{cog}}{l_\mu} \tag{3.3}$$

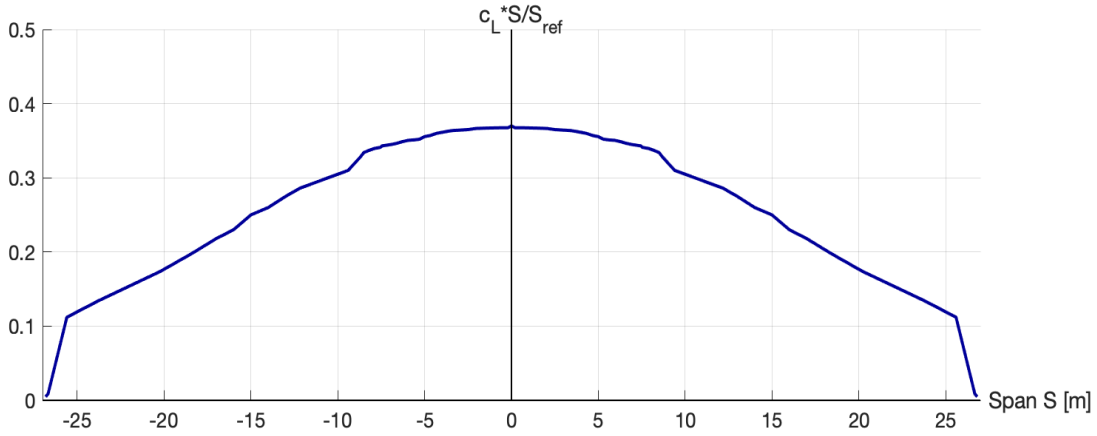

Figure 3.12.: Spanwise lift distribution

The aerodynamic analysis provides the polars of the BWB during take off (Figure 3.13) and cruise (Figure 3.14) respectively. The most important parameters like lift to drag ratios and maximum coefficients of lift are listed in table 3.5.

Table 3.5.: Aerodynamic Parameters

Parameter	Take Off	Cruise
$\frac{L}{D}$	27.48	26.7
c_{Lmax}	1.1	1.3

As a result of the mass breakdown, the center of gravity is calculated to be 16.65 m measured from the radome of the BWB. The resulting moment coefficient for cruise in figure 3.14 demonstrates, that both criteria for static stability are met. The static stability and the trimmed cruise flight at about 3° AoA were only achievable by introducing a V-shaped stabilizer. The V-shaped stabilizer was an adequate compromise between the reduction of lift to drag ratio and achieving directional in addition to longitudinal stability. Prior to the introduction of the stabilizer, large winglets were implemented to assure adequate directional stability. Now the winglets of the BWB can be simplified and shortened due to the fact, that their primary purpose is not to supply directional stability anymore. Their primary purpose now is to reduce the induced drag at slow phases of flight and to produce an optimized elliptical lift distribution across the BWB. In order to achieve longitudinal stability without the necessity of using a V-shaped stabilizer, the wing needs to be further optimized and state-of-the-art control surfaces need to be implemented [Wu+12]. This however, exceeds the scope of the current design study.

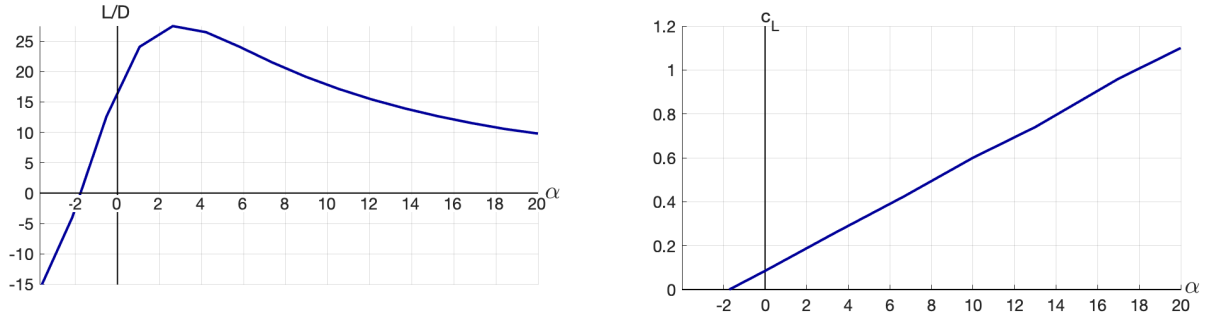

Figure 3.13.: BWB Polars during take-off

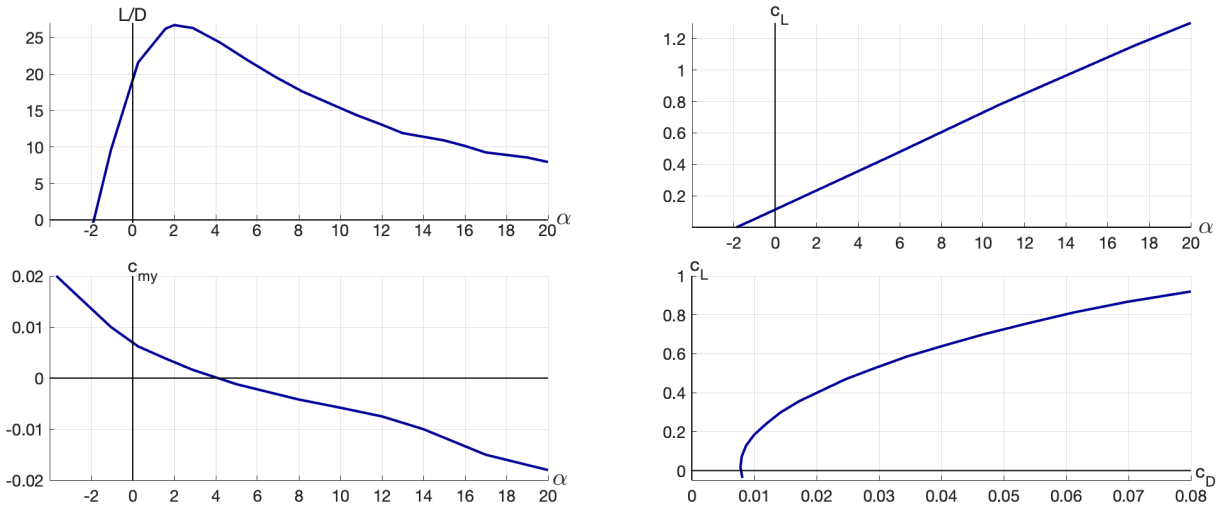

Figure 3.14.: BWB Polars during Cruise

3.3.2. V-n Diagram

The V-n diagram Figure 3.15 represents the load factor n versus airspeed V and is composed of both maneuver and gust loads. These are superimposed to fully demonstrate the flight operating strength of the airplane and the flight design frame. It shows, how the speed must be adjusted to account for various effects such as turbulence, stall, dive, etc [Gud13]. The dive speed $V_D = 310.1\ m/s$ represents the maximum speed the aircraft structure can safely withstand. The intersection of the positive limiting load factor and the line of maximum positive lift capacity is marked by the maneuvering speed $V_A = 63.59\ m/s$. $V_c = 221.5$ is the cruise speed and $V_S = 39.94\ m/s$ is the stall speed at a load factor of $n = 1$. The procedure is carried out based on the CS-25 [Age20]. Accordingly, the maximum positive load factor $n^+_{max} = 2.5$ and the maximum negative load factor $n^-_{max} = -1$ are obtained. Load factors due to gusts ranging from a negative 1.5 to a positive 3.5 are not unheard of as stated by [Ray18, p 497].

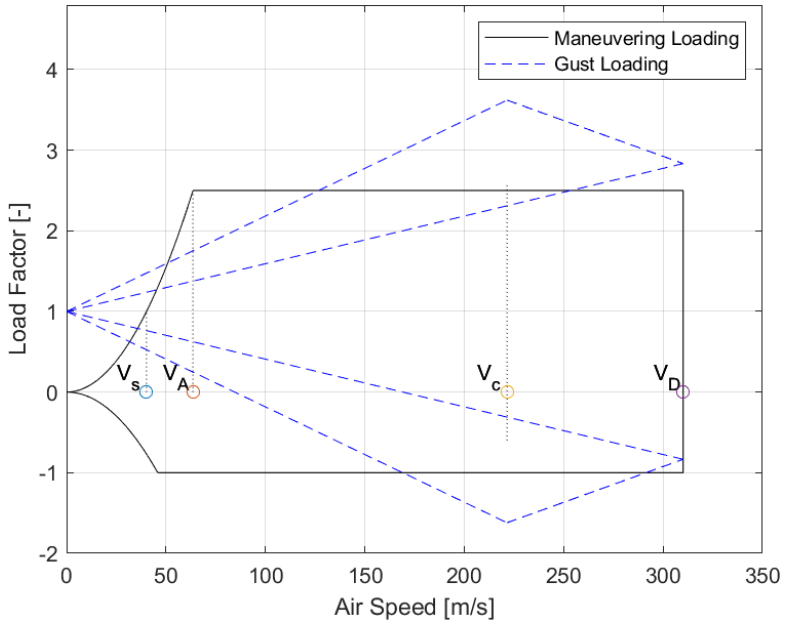

Figure 3.15.: V-n Diagram

3.4. Energy Calculation

In order to calculate the total necessary energy to complete the design mission, the energy consumption for the different individual systems is calculated. The energy requirement is the decisive factor for the design of the fuel cell and its many components, which is why a preliminary approximation is of great importance. The main energy consumer is the propulsion system. However, the other systems and subsystems that require electrical energy should not be overlooked nor underestimated.

3.4.1. Cabin Energy Requirements

For the cabin energy consumption, the values were obtained using an approach method based on data from literature [Sch15]. Electrical, hydraulic, pneumatic, and mechanical energy are the main types of energy in a conventional aircraft. The traditional ECS is powered mainly by bleed air extracted from the engines, hence it is powered by pneumatic energy. Wing Ice Protection System (IPS) is typically applied using hot bleed air extracted from the engines. It's main power source is also pneumatic energy. However, some components like cockpit windows and ice detectors use electrical energy for anti-icing. The landing gear and many actuators of the flight control surfaces (FCS) need hydraulic energy. Due to its difficulty to analyze every detailed energy system, it is assumed that the aircraft is an all-electric aircraft (AEA). To calculate the total energy consumption, the following five flight phases are taken into consideration: take-off, climb/accelerate, cruise, loiter, and descent. The results for the energy consumption are shown in table 3.6.

Table 3.6.: Cabin Energy Consumption per Segment [kW]

	Take-Off 0.02 h	Climb/Accelerate 0.11 h	Cruise 2.51 h	Loiter 0.46 h	Descent 0.22 h
ECS	150	150	240	240	150
Cabin and Cargo	96	96	127	127	96
Exterior Lighting	2.5	4	2.5	2.5	4
Avionics and Cockpit	4	4	4	4	4
Total Cabin	252.5	254	373.5	373.5	254
Anti-icing	0	62	3	3	62
Actuators of the FCS	0	72	72	72	72
Fuel system	6	6	6	6	6
Total Systems	258.5	394	454.5	454.5	394

3.4.2. Propulsion Energy Requirements

The thrust for flight is generated through a propulsion system consisting of electrical-powered propellers. The energy requirements for the propulsion system are obtained by taking into consideration multiple assumptions regarding the power strain. The design mission is set for a range of 2000 km at a cruise altitude of 6000 m at Mach 0.7 The propeller efficiency is set to 80% according to [Ray18, p.481]. Nevertheless, improvements in the propeller efficiency of up to 99.94% can be expected by 2030 [FB09].

For the electric motor efficiency, values between 90% [Ray18, p.739] and 99% [FB09] for the year 2030 were obtained. A realistic efficiency of 95% for the electric motor is assumed for the calculations. For the inverter/controller an efficiency value of 99%[Ray18, p.745] is set. The MTOM was first approximated according to the literature. As the energy requirements are obtained the mass for the energy generation system needs to be calculated again and the process is repeated. After multiple iterations, the system stabilizes and final results are obtained.

For cruise, the thrust was calculated using the thrust to weight ratio as from equation 3.4 taken from [Ray18, p. 120] with an $(L/D)_{\text{cruise}}$ equal to 26.7 at a cruising altitude of 6000 m as stated on 3.5. With the thrust needed for cruise, the mechanical energy was obtained using the equation 3.5 [Ray18, p. 483]. The electrical power required for the electric motor is then obtained using the motor efficiency. The resulting electrical

power is obtained by applying the inverter/controller efficiency as seen from equation 3.6. For the loiter flight phase, the process is similar as in cruise, taking into consideration that the $(L/D)_{\text{loiter}}$ is equal to 86.6% of $(L/D)_{\text{cruise}}$ according to [Ray18, p.120] at a loiter altitude of 4500 m. For the take-off a relationship between $(P_{\text{takeoff}}/D_{\text{cruise}})$ is estimated from [Ray18, p.122] to be between 40 to 70%. Comparing this to the value for the propulsion system used in the NASA N3-X aircraft [FB09], a value of 40% for $(P_{\text{takeoff}}/D_{\text{cruise}})$ is set for the MANTA. For the climb the CL_{max} was determined to be 1.3 as seen on table 3.5. With a climb rate of 3500 ft/min the necessary power for climb was calculated. For descend it was assumed that the electric motors are idle with a power between 8-10 % of the maximal power. The duration of each of the flight phases was either taken from literature or calculated using the speed and range. The results for the propulsion energy requirements can be found in table 3.7. For the total energy requirement, the cabin energy requirements (Table 3.6) and the propulsion energy requirements were added and the result is found in table 3.7.

$$\left(\frac{T}{W}\right)_{\text{cruise}} = \frac{1}{\left(\frac{L}{D}\right)_{\text{cruise}}} \tag{3.4}$$

$$P_{\text{mech}} = \frac{T}{\eta_{\text{prop}} V_{\text{cruise}}} \tag{3.5}$$

$$P_{\text{electric}} = \frac{P_{\text{mech}}}{\eta_{\text{emotor}} \eta_{\text{inv/con}}} \tag{3.6}$$

Table 3.7.: Energy Requirements for Thrust generation and Total

Flight Phase	Duration	Mechanical Power Propulsion	Electric Power Propulsion	Total Electric Power
Take-off	0.02 h	19.39 MW	20.61 MW	20.871 MW
Climb	0.11 h	17.37 MW	18.47 MW	18.865 MW
Cruise	2.51 h	8.10 MW	8.61 MW	9.066 MW
Loiter	0.46 h	9.22 MW	9.80 MW	10.255 MW
Descend	0.22 h	1.94 MW	2.06 MW	2.455 MW

3.5. Balanced Field Length

With the mass of the MANTA determined in subsection 3.1.2 and the aerodynamic characteristics obtained in section 3.3 the balanced field length (BFL) is calculated. The propulsion system (fans, e-motors, inverter/controller), as mentioned before in subsection 3.1.2, is obtained from the NASA N3-X aircraft [FB09]. The NASA N3-X aircraft is a good reference since it is also a BWB with an electrical propulsion system (31,000 ft at Mach 0.8). As the NASA N3-X aircraft is more than double the MTOM of the MANTA, the propulsion characteristics are calculated for each propeller. Comparing the required thrust and mechanical power for the different flight phases with the propulsion characteristics of the NASA N3-X propellers, it is determined that four of the NASA N3-X propellers satisfy the propulsion requirements of MANTA. The most important characteristics of the NASA N3-X propulsion system are summarized in table 3.8 [FB09, tab 4]. Figure 3.16 shows a simplified rendering of the propulsion system to get a better understanding of its shape and function.

The equation 3.7 and equation 3.8 are taken from [Ray18, p.675] and used for the determination of the BFL. The equations are empirical and therefore set in the imperial system and afterwards, conversions were undertaken.

$$BFL = \frac{0.836}{1 + 2.3G}\left(\frac{W/S}{\rho g C_{L_{\text{climb}}}} + h_{\text{obstacle}}\right)\left(\frac{1}{T_{av}/W - U} + 2.7\right) + \left(\frac{655}{\sqrt{\rho/\rho_S L}}\right) \tag{3.7}$$

$$T_{av} = 5.75\, bhp \left[\frac{\frac{\rho}{\rho_{SL}} N_e D_p^2}{bhp}\right] \tag{3.8}$$

With these parameters a BFL of 2413 m is obtained for the MANTA. With a typical electrical engine boost of 25%, according to [Ray18, p 739-740], a BFL of 1849 m can be achieved, satisfying the required BFL $\leq$ 2000 m. For landing, the stall speed $V_{\text{stall}} = 39.94\ m/s$ and the approach speed $V_a = 1.3 \cdot V_{\text{stall}} = 51.92\ m/s$ is obtained according to Raymer [Ray18, p. 676], satisfying the required approach speed of $V_a \leq 66.88\ m/s$.

Table 3.8.: NASA N3-X Propeller Characteristics

Parameter	Value	Description
P_{SL}	6.63 MW	Power at sea level
N_e	4	Number of props
D_p	1.285 m	Diameter of prop

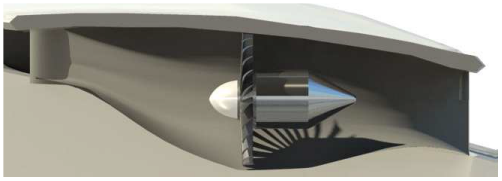

Figure 3.16.: Propulsion System NASA N3-X [FB09]

3.6. Structural Analysis

The aircraft wing is the primary lift-producing device of an aircraft. It bears aerodynamic and structural loads. In a horizontal steady flight, the principal loads acting are the weight, lift, drag, and thrust forces. However, in a realistic scenario, the airframe is loaded by a further combination of loads due to gusts, aircraft maneuvers, cabin pressure and landing gear. The loads can be either concentrated or distributed. The lift force and the weight act as distributed loads, whereas concentrated loads are applied to the aircraft by the landing gear and the thrust force. The consequence of either of the load cases acting on the structure can be seen in the form of deformation that correlates to stresses [Ald18]. This section explores the structural behavior of the outboard wing's (Sections A to C as shown in figure 3.4) load bearing structure. For the designed vehicle as shown in figure 3.3, a load-bearing wing skeleton comprising mainly of ribs and spars is modeled for the analysis. The final structure is obtained in an iterative manner and is illustrated in Figure 3.17 (a).

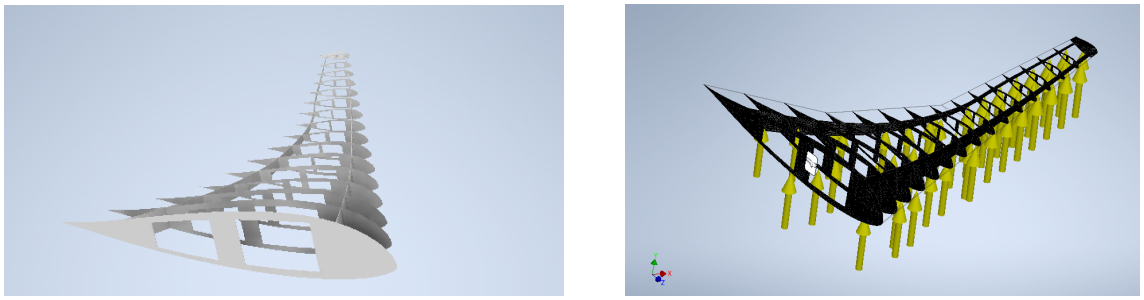

(a) Wing Load bearing structure

(b) Simulation Setup

Figure 3.17.: FEM Analysis

The modeling and the stress analysis of the load-bearing structure (Figure 3.18) are performed in Autodesk Inventor. The analysis interface in Autodesk Inventor requires the user to assign a material to the model, place forces and constraints for appropriate simulation results. As mentioned in Figure 2.1, GLARE is the material of choice for the MANTA concept due to its well-known advantages. As boundary conditions, the face of the wing at the root is set as a fixed constraint. Based on the mass calculations in section 3.1, the required lift force is calculated. Zhenli, C. et al states that the center-body of a BWB typically provides about 30% lift at cruise when an elliptical lifting distribution in the span-wise direction is assumed [Zhe19]. Based on the stated remark, the total lift force acting on the outboard wing is determined. The resulting force is then defined in the analysis interface as a distributed loading acting on the wing's lower panel. Once these parameters are defined, a fine mesh is generated. Figure 3.17 (b) shows the force distribution, the constraints and the mesh applied on

the wing structure. Thereafter, the structural analysis is performed, and the deformation is computed. The load-bearing structure is then optimized by reducing the rib and/or the spar width based on the computational results and the analysis is repeated. The deformation of the final iteration computed based on the stress analysis is provided below.

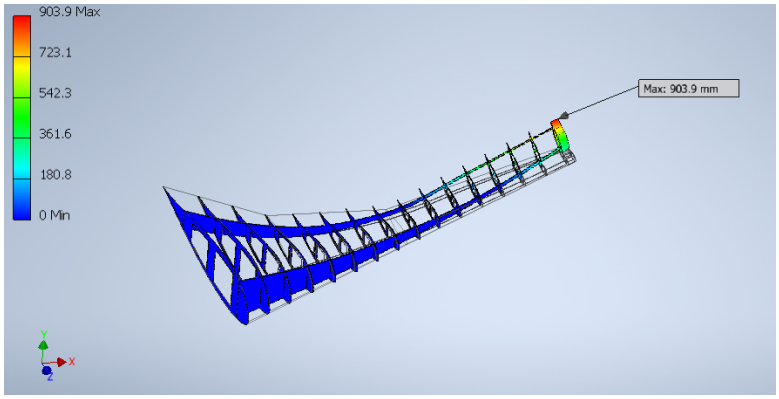

Figure 3.18.: Total Deformation

Spars sustain large loads inclining to twist the wing while the ribs prevent the wing from buckling. As can be seen in the 3.18, distortion is observed at the tip of the wing, calculated to be 903.9 mm. At the root of the wing, the deformation is minimal.

It must be noted, that the entire structure is modeled as a single solid body, hence the joints have zero clearance between them. The overall results show that the value of total deformation is minimal and the objective to obtain the static structural characteristic for the vehicle concept requirements has been achieved. Moreover, the increased stiffness observed near the root area in the wing section gives an insight into further the optimization potential. The structure can be further optimized by removing material from areas with minimal stress. This would consequently result in a reduction of aircraft weight and an enhanced aircraft performance.

3.7. Geometrical Representation

MANTAs geometrical representation of the front and side view are depicted in figure 3.19 and figure 3.20 respectively. More on the geometrical representation can be found in figure C.1 and figure C.2 as well as in table 3.9.

Table 3.9.: Geometric parameters MANTA

Parameter	Value	Description
L	36 m	Length
b	53 m	Wingspan
$Hmax$	7.2 m	Maximum Height
$Hwing$	3.8 m	Height under Wing
$Hdoor$	3.9 m	Height main Door

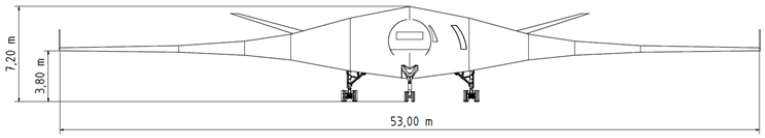

Figure 3.19.: Front View

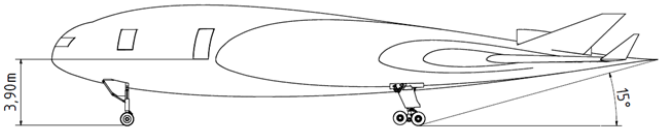

Figure 3.20.: Side View

4. Power Generation

4.1. Hydrogen Propulsion

For hydrogen propulsion, there are two possibilities for the usage of the fuel: First is the conventional combustion of the fuel inside a gas turbine, whereas the second possibility is the electric charge generated inside a fuel cell. Even though both technologies do not produce CO_2, hydrogen combustion produces NO_x because of the high temperatures generated. Additionally, fuel cells have a higher efficiency which led to the selection of fuel cell technology for the propulsion of the MANTA. The main property of the propulsion system is the amount of power to be generated. Through aerodynamics, the maximum electrical power requirement was calculated to be 20.87 MW during takeoff (Table 3.7). Regular jet engines aviation safety regulations mandate an extra of 25% to take the critical scenario of OEI into account [Ray18, p.739]. For the MANTA and other aircraft, which have a power source different from the engines, this critical scenario is shifted to that respective source. For redundancy, the fuel cell stacks are split into two independent subsystems. The OEI scenario is thereby applied to the power source raising it to approximately 26.1 MW.

4.2. Electric Components

Before the fuel cell can be looked closer upon, the APU has to be considered first. As mentioned before, the maximum power requirement is needed during takeoff for a very brief moment, while the power requirement is only at 9.07 MW for most of the flight. To reduce the sizing requirements of 100% of takeoff power, to the power needed during cruise, a battery is built into the system. In addition to providing a power boost of approximately 11.8 MW during takeoff and climb, the battery has the function to start the fuel cell system, as it cannot start without an external power source in a reasonable timeframe. Moreover, it has to fulfill the conventional requirements such as emergency door system, floor escape path lighting, emergency locator transmitter (ELT), Flight Data Recorder (FDR), and Cockpit Voice Recorder (CVR). Similar to the fuel cells, the battery is split at least into two independent units and 125% oversized for an OEI scenario. Consequently, the battery has to have a stored energy amount of approximately 1.8 MW h. The sizing parameters of such a battery [BD15, p.22] are selected after NASA SUGAR with an EIS of 2030-2035 and listed in table 4.1. The electricity generated by the fuel cell has to be converted for further usage which warrants a DC/DC and DC/AC converter. Both types are high-power SiC-based converters with 98%-efficiency or higher [Fra15] [Li+21] [Tay+20].

Table 4.1.: Battery characteristics

Parameter	Value
power	11.8 MW
energy	1.8 MW h
specific energy	750 $^{Wh}/_{kg}$
weight	2393 kg
specific cost	80 $^{\$}/_{kg}$
efficiency	97%

4.3. Fuel Cell

After the fundamental propulsion technology is set, the specific fuel cell type has to be selected. Amongst those, the proton exchange membrane fuel cell (PEMFC) and the solid oxide fuel cell (SOFC) are the ones with the most promising characteristics [Spe13, p.4] but the very high working conditions of the SOFC (800 °C) [Spe13, p.7] pose major difficulties. One of those characteristics is, that these fuel cells do not require pure oxygen and can work with air. Currently "in aircraft application, PEMFCs, which are more advanced, are a few steps ahead of SOFCs" [Fer+18, p.19], which sets the MANTAs source of power on a PEMFC. To get accurate sizing parameters, the PEMFC is based on a currently available model [Pow21]. The required power remaining after the boost is approximately 9.07 MW which results in 11.34 MW including the OEI extra. As the EIS is set to be in 2035, the PEMFC is calculated with an improvement of 10%, to represent the improvements in stack power density from 2021 to 2035, set by various fuel cell expert assessments [Whi+19, fig. 1C]. The fuel cell efficiency would thereby rise from the current model's 53.47% to 58.82%.

From the specified model the operating characteristics are specified in table 4.2. The optimum operating air pressure is around 2.5 bar [BM10, fig. 6] [Löh11, fig.6.4.2-1], but is limited to only 2 bar. The air temperature is set to 70 °C, as the increase in efficiency gets diminished by the dehydration of the membrane, leading to increasing ohmic resistance [Lar+18] [Löh11, fig.6.4.1-2]. The air humidity target is set to 80% because it causes the lowest drop in cell voltage [KCK15, fig. 7]. The oxygen excess ratio is set to 1.8, producing the highest cell voltage [BM10, fig. 6]. Through the chemical equations and characteristics given, the airflow required can be calculated to be approximately 12.43 $^{kg}/_{s}$. Coupled with the flight mission time and power required during different phases of the flight, the required hydrogen mass can be calculated to be 1276 kg which is shown later in equation 4.3. The operational lifetime is specified by the manufacturer to be 20 000 h. This value is very problematic, as it does not include the limit below which the fuel cell is considered to be nonoperational. The assessment made by fuel cell experts, defined the durability "as the time until the fuel cell stacks rated power reduces to a value that is 10% less than its beginning-of-life rated power", which will have risen from around 5000 h in 2020 to 6000-7000 h in 2035 [Whi+19, pp.4900-4901].

Table 4.2.: PowerCellution® P-Stack characteristics [Pow21]

Parameter	Value
max power	125 kW
cell count	455
volume	38.13 L
weight	42 kg
max H_2 pressure	2.2 bar
max air pressure	2.0 bar
operational lifetime	20 000 h

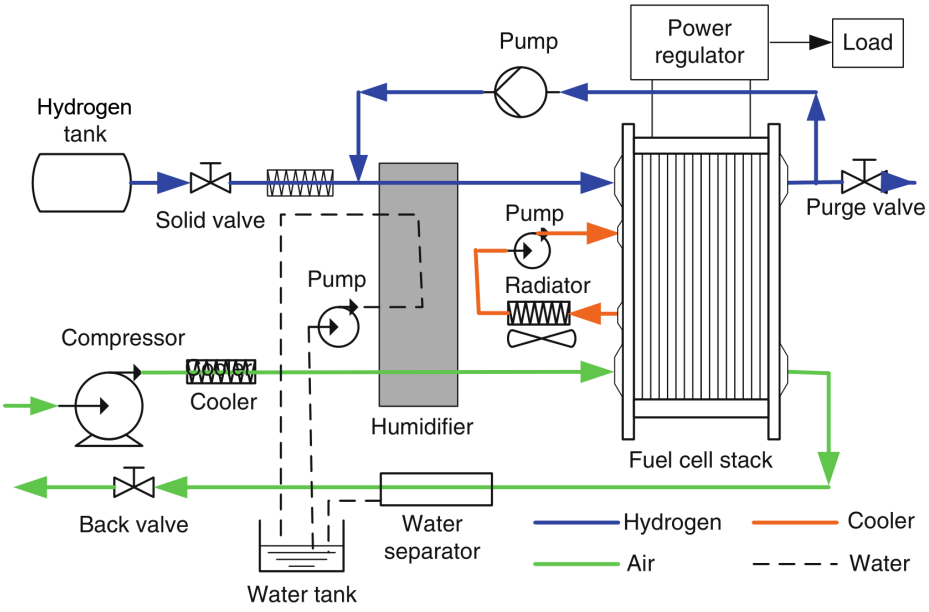

Figure 4.1.: Fuel cell system overview [Guo+13, fig.1]

4.4. Compressor

The first component's objective is to supply the fuel cell with 2 bar of air. However, due to the characteristics of the PEMFC, the compressor has to meet several additional requirements. The first requirement is to pressurize the air up to the above-mentioned optimum working conditions. The next requirements are mass and volume of the compressor which are shared between all aircraft components. Furthermore, the membrane requires an oil-free compressor as the oil would contaminate the membrane and damage it. The last requirement is the creation of pressure ripples which have to be limited to 100 mbar to 200 mbar because stronger ripples would rupture the membrane. In a comparison between several compressor variants the centrifugal compressor excels in most requirements which can be seen in the radar charts in figure 4.2 [BM10].
The next task is the polytropic calculation of the thermodynamic properties of the air compressor. The boundary conditions are the flight altitude of 6000 m which equates to a static air pressure of approximately 0.47 bar and the flight speed of 0.7 Ma, which equates to a dynamic air pressure of 0.54 bar. Similarly, the dynamic air temperature is 259 K.

To calculate the air compression in a realistic polytropic way, the compressor efficiency is needed. This value is specific to a compressor model which can be read off a compressor map which is usually provided by the manufacturer. With a conservative estimate of 75% [CR06], the polytropic coefficient and subsequently the polytropic ratio is calculated. With this ratio, it is possible to calculate the exit temperature of the air which results at 426 K. As a result, the compressor needs 2.1 MW which has to be provided by the fuel cell itself. This results in an iterative loop which increases the power to be generated from the fuel cell until the actual power generated meets the demand of the propulsion, the cabin, etc., and the parasitic demand of the compressor. Thus, the required power rises to approximately 14.2 MW. The parasitic power demand of 15% is the upper limit for air compressors in fuel cell systems inside regular environments [Zha+14, sec.1]. The next step is the mass of the compressor which is calculated with the specific values of the air sub-system of a fuel cell from Ballard [Bal21]. This results in a mass of 1271 kg for the compressor including a motor to drive the compressor. The entire compressor calculation is done without any future improvements for the sake of more realistic values instead of non-established concepts. One of many future improvements would be the use of blade-less turbo compressors [HW17] or air-foil-bearing motors produced from Mohawk Innovative Technology [Moh21] which would significantly improve the motor efficiency.

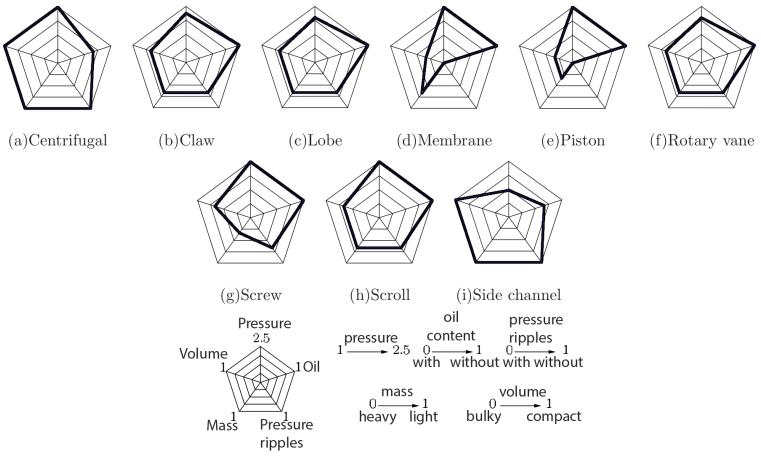

Figure 4.2.: Radar chart of different compressor variants and their corresponding properties [BM10, fig. 9]

4.5. Heat Exchanger

Once the air is compressed the temperature will exceed the maximum temperature of the fuel cell membrane. Moreover, the fuel cell and the compressor efficiencies are less than perfect which implies that waste heat is generated. For all of those reasons, a heat exchanger has to be build into the system to cool off these components. As it is explained in later sections, the cryogenic hydrogen plane has the advantage over the regular kerosene airplane, that there is a mass that has to be heated to the operating conditions of the fuel cell. These tasks can be synergized together to vastly reduce the size of the heat exchangers that would be required. The heat exchanger type is selected to be a cross-flow heat exchanger as it fits the requirements of an aircraft better than a counter-flow heat exchanger. The specific model is set to be a louvered-fin heat exchanger to increase the effective heat transfer area [Lüd+11, p.1092]. The heat exchanger is calculated with the ε-NTU Method whereas the ε is not calculated but taken from empirical data [CW97]. This is because even a simplified heat exchanger is dependant on multiple geometric assumptions such as the tube height, -length, -wall thickness, fin height, -length, louver angle, louver cut length, etc. The ε-NTU equation for an unmixed cross-flow [Hes01, Table 6.1]:

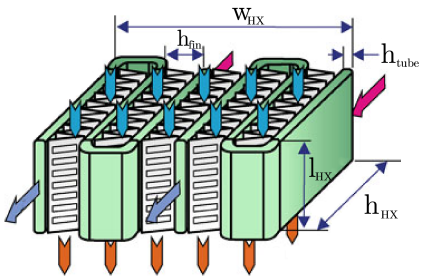

Figure 4.3.: Louvered heat exchanger segment [LST13, fig.18]

$$0 = \varepsilon - \left\{1 - \exp\left[\exp\left(-\mathrm{NTU}^{0.78} \cdot C^* - 1\right) \frac{\mathrm{NTU}^{0.22}}{C^*}\right]\right\} \tag{4.1}$$

In addition to the geometric assumptions (Table D.7), there are also multiple assumptions over the heat transfer known as the Murray-Gardner Assumptions [Mur38]. The mass of the heat exchanger is susceptible to major increases of up to 100% due to redundancy considerations [Kel+21].

4.6. Water system

After the air is cooled down, it has to be humidified. This is accomplished by a humidifier, of which there are three installation variations. Even though the cell-internal humidifier is the most efficient regarding water and power consumption [Bra12], MANTA uses a cell-external humidifier, as the scope of this project is time-limited to the overall-aircraft design level. The main design aspect of all water-related components in the fuel cell system is the water mass flow. The water mass flow is dependant on air volume, air temperature and the humidity level to reach. As a result of the pressurization in the compressor and the cooling in the heat exchanger, the air has a pressure of 2 bar and to 70 °C. The humidity to reach equals 80%-relative, which can be inserted into the Magnus-formula to calculate the saturation vapor pressure of water [Ver16]:

$$E_{\text{saturation}} = 5.95\,\text{hPa} \cdot \exp\left(\frac{16.819 \cdot \vartheta}{227.3163\,°\text{C} + \vartheta}\right) \tag{4.2}$$

The vapor pressure can be used to calculate the partial pressure of water, after which the absolute water mass is calculated. The water mass flow rate for the given air properties and volumetric flow rate of approximately $7.84\,\text{m}^3/\text{s}$ equates to approximately $1.61\,\text{kg}/\text{s}$. The same formulas can be used to calculate the incoming water at the flight altitude, however, this results in very minor quantities which match the ICAOs ISA model assuming dry air. As they are not mass-critical components, sensors and controllers are not explicitly mentioned in this report, however, their importance is of utmost. As an example, the water system has to be controlled, as a too-minute amount of water would lead to membrane dehydration, and a too-high amount would lead to water flooding which would block the gases from the catalyst. For the type of humidifier, there are two considerations: The first is a mechanical nozzle spray humidifier, and the second a membrane humidifier. While membrane-type humidifiers are more suited for automobile applications and have a system efficiency, the decision is made on a nozzle spray humidifier as membrane humidifiers have insufficient humidification performance for high power applications [Cha+18] [CP05]. To verify the mathematical calculations on real-world data, a specific model is selected [Hyg17, HPS].
After the humid air reaches the fuel cell, the cathode-side gets humidified. Following this, the anode-side is humidified too as the water diffuses through the membrane. Because the anode side is filled with pure hydrogen, this educt is recirculated into the inflow of the fuel cell. In contrast, the cathode side is filled mostly with unwanted gases, which have to be discharged out of the system. However, this oxygen-starved air still has water in it, which has to be separated to be recirculated into the humidifier before the fuel cell. For this application, there are multiple methods of separation such as a centrifugal water separator and a water condenser. MANTA uses the centrifugal-type water separator which has low energy consumption and high separation efficiency. Likewise other components, the water separator is based on practical data [CF 17, Parker/Hiross Model SFH209]. The last components necessary are a simple water pump and a water tank. The pump has to move the water from the separator back to the humidifier, while the water tank is placed in between them, to be a buffer for the start process of the fuel cell system.

4.7. Hydrogen Storage

One of the biggest challenges of hydrogen-powered aircraft is the storage of hydrogen. Even though it only weighs approximately one-third of kerosene, it requires a four times larger volume in a liquid state for the same amount of energy. To reach a liquid state, hydrogen has to be cooled down to 20 K which creates the demand for high thermal insulation along with regular mechanical stresses in pressure vessels. Before it is possible to calculate the thermal insulation, the size of the tank to be surrounded with has to be calculated first. This size is dependant on the mass to be stored, the temperature it is stored at, the pressure inside the tank and the ratio between liquid and gaseous fluid. The mass to be stored is calculated with the combination of the fuel cell properties and the corresponding flight mission data [Kab21]:

$$m_{\text{H}_2} = \frac{n_{\text{cell}} \cdot n_{\text{stack}} \cdot I \cdot \lambda_{\text{Anode}} \cdot M_{\text{H}_2} \cdot t_{\text{total}}}{2 \cdot F} \cdot \left(\frac{t_{\text{TO}}}{t_{\text{total}}} \cdot \frac{P_{\text{TO}}}{P_{\text{max}}} + \frac{t_{\text{Climb}}}{t_{\text{total}}} \cdot \frac{P_{\text{Climb}}}{P_{\text{max}}} + ...\right) \tag{4.3}$$

This results in a mass of 1276 kg hydrogen for Mission profile 2 and 666 kg for Mission profile 1.

4.7.1. Mechanical Design

After the mass is calculated, the density has to be specified to calculate the volume. As mentioned above, the liquefaction at 1 bar occurs at 20.23 K. Between the cryogenic fluid and the ambient surroundings there is a temperature difference of more than 250 K, which leads to boiling the liquid hydrogen back into its gaseous state. Consequently, the pressure rises inside the tank which is the reason the tank is designed for burst pressure of 2 bar. The design burst pressure is kept at a relatively low value to keep the tank weight low. One of the characteristics of hydrogen is, that the atoms are so small, that they diffuse inside and out of the tank walls. To counteract this problem the tank material has to be made out of a metal which leads to significantly slower permeation [Ver13]. Aside from the metallic property, the tank material has to have a low value of heat conduction and as usual low weight. Linde, a company specialized in pressure vessels, sells liquid hydrogen tanks which use Cr-Ni-steel as tank material [Lin13, p.5], however, in the weight-sensitive application in aircraft, steel and different steel alloys drop out of the selection. Another consideration is titanium as it has roughly half the density and additionally a much lower heat conductivity. Nevertheless, titanium suffers heavily from hydrogen embrittlement which makes it also drop out of the selection. Liquid hydrogen has been used for decades in spacecraft which led to many studies being made on the best hydrogen tank materials by NASA. The material used in the external tanks of the space shuttle was the aluminium alloy Al-2219 [Nat05]. On the one hand, aluminium is very resistant to hydrogen permeation and has a low density but on the other hand, it has a high heat conductivity [Oeh09]. This is not a big problem, as the problems of the other materials, which is the

Table 4.3.: Tank design parameters Mission 2

Parameter	Value
n_{Tanks}	4
p_{Burst}	2 bar
$V_{\text{Hydrogen,single}}$	7 m^3
$V_{\text{Cylinder,single}}$	20.22 l
$V_{\text{Klöpper,single}}$	1.84 l
m_{single}	64.52 kg
m_{total}	258.1 kg

Table 4.4.: Approximate tank material comparison [Ran14] [Don00] [PGW14] [AWK19] [Con17]

Parameter	Density	E-Modulus
Cr-Ni-Steel	7500 kg/m^3	219 GPa
Titanium	4500 kg/m^3	105 GPa
Al2219	2825 kg/m^3	72 GPa
Al-Li 2195	2700 kg/m^3	78 GPa

reason the MANTAs tanks were first considered to be made out of this alloy. However, after further research Al-2219 is replaced with Al-Li 2195 which is also used by SpaceX Falcon 9 [Spa07] [bVS07, p.8]. The newer alloy has increased strength with lower density [MS10] which makes it even more suitable for the MANTA [R P+91] [Ver13]. Another additional advantage of using a material that is particularly researched for cryotanks is that the mechanical stress calculation requires the material characteristic properties e.g. e-modulus at those temperatures [KP15].
After the material is set, the next step is the specification of the tank form. The optimal tank form is of spherical shape which has to be changed befitting the constraints of the BWB. A very good compromise is to elongate the form into a cylinder and end it with dished bottoms also known as the Klöpperboden. The AD2000, a regulation for pressure vessels of the German TÜV, is used to calculate the necessary wall thickness.

4.7.2. Thermal Design

After the inner shell of the tank is calculated, the next step is the calculation of the outer insulation layer. Identically to the inner tank, the selection of the material is of utmost importance. The most important properties to be considered are the density of the material, which will determine the weight, the heat conductivity, which will determine the heat losses and hydrogen permeability, which might lead to embrittlement [Raj+13]. Insulations to be considered include vacuum insulation, different foam types and aerogels. The aforementioned Linde company uses powder-filled vacuum insulation which offers near-zero heat conductivity, however, its additional weight and safety considerations take this form of insulation out of the selection [Lin13]. "Aerogels offer some of the lowest reported thermal conductivity values for any solid" but due to its relative novelty among other insulations, it hasn't been tested enough to be considered for airborne cryotanks.

"A major problem with the use of aerogel granule insulation has been that thermal performance is worse than that of a monolith because of gas-phase conduction in intergranular regions"[SMB98]. Fortunately foams are well established, have low costs and have low density. The notable compromise is that foams have higher heat conductivity relative to the other options [Ver13, chp.3]. Moreover, the foam has to be coated with an air impervious layer as air will reach the outer tank wall and freeze on it. Outside of valid safety problems the frozen air would compromise the functionality of the thermal insulation. Accordingly to the establishedness, there is a huge variety of foams from which there has to be selected. A suitable foam is closed-cell polyurethane, which offers a heat conductivity of 0.1 $^{W}/_{Kh}$ [Bre91, chp.7.4.3.] [Nat77]. After the insulation material is set, the next step is the calculation of the foam thickness and subsequently the insulation mass. As figure4.4 shows, the main purpose of the insulation is to minimize the mass flow going from liquid hydrogen to gaseous hydrogen. To reduce this symptom, the heat flow from the environment to the hydrogen has to be minimized. The design of the thickness is thereby set to achieve a heat flow after which a relative value of the hydrogen will be evaporated. The boundary constraints on the calculations are the heat flow from the environment e.g. a hot day on a hot airport such as Dubai. The design parameter of evaporation is set to 5% and the time is set to 12 h. Now an iterative loop is constructed with the isolation thickness as the iteration variable, which will be increased until the evaporated mass is below the design parameter of 5%-relative. As a result, a thickness of 15.4 cm is calculated. The fuel line calculation is very similar to the tank calculation, as both of them have the same material constraints, environment, same fluid flowing through them. The main difference is that the size of the tank is designed for the entire need of hydrogen across whereas the pipes are designed for the mass flow required for the fuel cell.

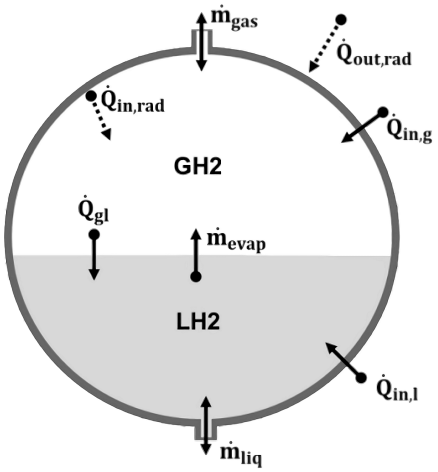

Figure 4.4.: Thermodynamic tank model [Dan+19, fig.3]

Table 4.5.: Thermal tank calculation parameters

Parameter	Value
Time on ground	12 h
ϑ_{Env}	50 °C
λ_{wall}	130 $^{W}/_{mK}$
λ_{iso}	0.0137 $^{W}/_{mK}$
ρ_{iso}	35 $^{kg}/_{m^3}$
Isolation thickness	15.4 cm
$m_{iso,total,empty}$	890.55 kg

4.7.3. LOX Storage

During the first design considerations of MANTA, a liquid oxygen tank was considered. This is due to the parasitic power demand of the compressor. If pure oxygen could be delivered to the fuel cell, it would allow a power boost, which would be used during power peaks such as the takeoff. The power boost would cause the downsizing of the compressor and moreover, it would lower the overall power demand and thereby the hydrogen demand as the parasitic energy demand of the compressor would be missing. The results of the initial sizing phase and comparisons with LOX variants are shown in table D.6. After the considerations of a battery as the APU, the battery and additional components would be oversized for usage as a power boost parallel to the fuel cell. As the battery skips the fuel cell, unlike a LOX Tank and the additional problems of liquid oxygen itself such as the cryogenic temperatures and acquisition of it pose major disadvantages compared to a battery.

Table 4.6.: Fuel line design parameters

Parameter	Value
Length	25 m
p_{Burst}	2 bar
d_{inner}	2.5 cm
$\dot{m}_{H_2}$	0.21 $^{kg}/_{s}$
Isolation thickness	15 cm
$V_{Cylinder,single}$	20.22 l
$V_{Klöpper,single}$	1.84 l
$m_{wall,total}$	17.97 kg
$m_{iso,total}$	12.98 kg

4.8. Hydrogen Safety

The switch to hydrogen fuel necessitates a close look at operational safety. Besides chemical problems like the difference of inflammability, combustion and fire extinguishing, public opinion has to be considered as well. For the purpose of sustainability the European community majorly funded a project under the name of *Cryoplane*. The project was coordinated by Airbus Germany with many partners such as the Hamburg University of Technology, the German Federal Institute for Materials Research and Testing, Cranfield University, the German Aerospace Center, Linde AG, Fraunhofer Society and many more. One of the aspects of this project was hydrogen safety in which the items examined were disk burst, lightning strike, bird strike, emergency landing, fire protection and fuel system. "The analysis concluded that from a safety point of view there is no fundamental problem, which would prevent the successful operation of a commercial aircraft running on liquid hydrogen. [...] In general terms, the conclusion is that Hydrogen poses its specific safety aspects to be considered in design and operation. However, the overall safety level will not be worse than for kerosene aircraft."[COR03, sec.4.5] According to these results the tank and propeller positions are constrained to not overlap. The tank area and the cabin area are two completely separated spaces. The tanks have build-in pressure release valves, in case the tank area is breached and suffers a pressure loss which could lead to too-high mechanical stress. According to this scenario, a sensor would measure an irregular pressure change in the tank and open a flap to disperse the gaseous hydrogen into the atmosphere and close after the tanks have reached a non-critical pressure level.

4.9. Airport infrastructure

The feasibility of hydrogen aviation is dependant on the fuel supply which has to be integrated into airports. The supply requirement can be split into the distribution and the storage of hydrogen. The storage of hydrogen in airports can be realized similarly to the aforementioned long-term storage Linde AG tanks. Those will ensure minimal evaporation losses, however, the main problem is how the liquid hydrogen is supplied to those long-term tanks. The distribution options can be differentiated between internal to the airport and external hydrogen production. Should a large hub be close to a large enough water source it would be beneficial to create an on-site hydrogen production, as that would eliminate transportation costs. The more common option will be external hydrogen production which can be further differentiated into liquid or gaseous hydrogen transportation. An external large-scale liquefaction with current standards is able to produce $25\,{}^{t}/_{day}$ LH_2 [Car18]. Should the hydrogen be delivered in a gaseous-state there would have to be an internal liquefaction plant [Ver09, sec.A4]. For this exact purpose, a competition under the name *H_2 HUB AIRPORT* was held by Airbus, Air France-KLM, the Île-de-France Region, and others for companies to apply and undertake parts of the hydrogen supply chain [Cho21]. The eleven winners include Air Liquide, which has developed a refueling truck with a large liquid hydrogen capacity, Geostock, who are specialized in underground energy storage solutions, and Hydrogen for Airport Handling, which designed hydrogen-powered ramp vehicles.

5. Operations

5.1. Flight Emissions

One of the main advantages of hydrogen fuel is the elimination of the pollutants, which are emitted in conventional aircraft engines such as SO_x, NO_x, CO, CO_2 and other unburned hydrocarbons. The only substances emitted from an electrochemical-powered aircraft are H_2O and oxygen-depleted air. H_2O is a greenhouse gas comparable to CO_2, but a key difference is the residence time in the atmosphere which is around 100 years up to thousands of years for CO_2 and only a couple of weeks up to 9 months for H_2O[NDN09, Fig.5]. For this reason, water vapor is generally considered harmless, however, this only holds true if the water vapor is not emitted in the upper stratosphere or above [MJE04, Sec.6.4.2]. The stratosphere starts at 8 km at the poles and at 18 km at the equator [Lab99]. The emitted water vapor causes two effects: the first is an increase in the radiative forcing and the second is the formation of contrail. The change in radiative forcing is negligibly small [NDN09, Fig.9], while the consequences of the contrails are more complex and are under ongoing research. An up-to-date view on this matter is published by the DLR under the umbrella of the EXACT project, which gives an explanation to contrail formation and subsequent climate impact. The author states that the water emitted by a fuel cell-powered aircraft causes contrails much easier than a jet engine-powered one. This is caused by differences in exhaust temperature and emitted water amount. Apart from the ease in creation, the fuel cell-created contrails will mostly be short and "not have any noticeable impact on weather and climate". However, the author concludes his assessment with a statement that the theoretical work has to be verified by numerical experiments and research flights [Gie21, pp.164-165]. For those reasons, MANTA cruises at 6 km where the potential consequences are expected to be greatly reduced.

5.2. Cost Analysis

This section provides a life cycle assessment of the MANTA aircraft concept. The aim is to assess its economic benefits and commercial viability, given that the airlines and manufacturers are profit-oriented entities. A novel concept such as MANTA which is a hydrogen fueled aircraft would require a significant amount of investment to reach from a preliminary design stage to that of commercial use. Life cycle cost (LCC) concerns with the overall cost of a product from its inception up to disposal. Apart from the acquisition cost, the direct operating cost (DOC) and the indirect operating cost (IOC) are the major components that are included in the LCC. The DOC is directly based on aircraft characteristics and type whereas the IOC is more dependent on other factors such as the airline's strategies. Within the framework of this report, the focus lies on the life cycle evaluation of hydrogen fuel-based aviation and the costs from the airliner operator perspective which include the acquisition cost as well as the operation and maintenance costs. The direct operating costs consider fuel, maintenance, crew salary, depreciation, insurance, etc. Using conventional methods, an initial prediction of costs can be made based on assumed values. Following the initial sizing section 3.1 and the established performance characteristics of the aircraft, the development cost and DOC are determined using the DAPCA (Development and Procurement Costs of Aircraft Model) IV Model described in [Gud13]. The calculations are performed based on the expected weight of the bare air-frame and maximum level airspeed. The table below outlines the components considered in development costs and provides the total costs obtained.

The values stated in the table are obtained under the assumption that the pressurized aircraft to be certified under the 14 CFR Part 23 and will feature a tapered wing with a simple flap system. It can be assumed that the aircraft concept will largely constitute composites in its construction. The entire cost estimation indicates a minimum selling price of at least \$162M. Each element of the cost will be reduced using the learning curve, which implies that the manufacturing cost of an aircraft will reduce as more experience is gained. The aircraft concept is targeted to enter service in 2035. Considering an inflation rate of 3%, the minimum selling price of the aircraft is estimated to be \$230M.

Following the same calculation model, the direct operating costs are estimated and an hourly cost of about \$8100 is computed, assuming 3000 flights per year. The assumed number of flights per year is determined based on the mission duration and while taking into account maintenance periods, night flying restrictions, time for route planning etc. The cost accounts for maintenance, engine overhaul, storage, load repayment, fuel costs, and crew costs. The annual loan repayment costs are included assuming that the aircraft is partially funded through financial institutes and paid out over a duration of 20 years. This is accounted for using the standard mortgage formula. As the aircraft is hydrogen-fueled, the fuel costs are estimated by assuming the specific fuel price of

Figure 5.1.: Development Costs

Parameter	Cost per Unit [million USD]
Engineering	9.500
Development Support	0.470
Flight Test operations	0.088
Tooling	2.520
Certification	12.578
Manufacturing labor	10.000
Quality Control	1.820
Materials/Equipment	0.980
Propulsion System	140.000
Avionics	0.620
Total Cost to Produce	162.24

Figure 5.2.: Direct Operating Costs

Parameter	Cost per year [USD]
Maintenance	76 380
Storage	12 000
Annual Fuel	8 046 000
Crew	960000
Annual Insurance	2 300 000
Annual Inspection	15 000
Engine Overhaul Fund	60 000
Annual Loan Payment	12 887 000
Total yearly cost	24 340 000
Cost per Flight Hour	8115 $/h

hydrogen fuel of $6/kg [Cou20]. Typically fuel costs account for about 30% of total direct operating costs. The fuel cost here encapsulates all costs to produce the fuel and the required infrastructure for distributing, storing, and refueling the airplanes. Given the current cost of hydrogen technology and limited infrastructure, it cannot compete against conventional alternatives for the cost of similar payload capacities. However, hydrogen fuel prices are predicted to lower significantly in the coming years as production technology and infrastructure for liquid hydrogen fuel improves and becomes more accessible. Total maintenance costs might rise due to larger airframes owed to the LH_2 tanks in the initial years of introducing such novel concepts. In the long term, however, the maintenance cost will decrease. Other costs such as increased airport and Air Traffic Control (ATC) fees due to increased take-off weight. Assuming an increase in refueling time for a hydrogen-powered aircraft, the turnaround time would increase, which would imply fewer flight cycles. By 2035 however, there would likely be better hydrogen supply infrastructure in place. Refueling trucks carrying LH_2 are also a viable option. At scale by 2035, the cost of LH_2 may be as low as $2.60 to $3.50 per kilogram. The cost difference between the envisioned hydrogen-fueled aircraft concept and a conventional aircraft could then substantially reduce for short-range flights. [JJ20] The most important benefit of hydrogen fuel is that it is carbon neutral. The use of hydrogen fuel cells produces only water vapor. This makes hydrogen favorable from an ecological point of view and in the future, the economic benefits of the same are foreseeable as such novel concepts can potentially allow airliners to pay decreased emission taxes. The cost model used here does not include climate impact abatement costs. The overall environmental benefit and the argument of hydrogen fuel being carbon neutral however depends on the method of production. Catalytic gas reforming, high-temperature pyrolysis, and water electrolysis are widely used methods for hydrogen fuel production. Out of all water electrolysis is considered to have the lowest carbon footprint. Its carbon footprint strongly depends on the source of electricity. The cost assessment in [JJ20] shows that in the years leading up to the complete availability of hydrogen fuel supply system and infrastructure, the costs per flight and carbon abatement costs will be higher, as this novel concept would necessitate new aircraft designs and infrastructure. Assuming that hydrogen propulsion is adopted widely, the abatement costs for a short-range mission of 2000 km could be as low as $70 to $130 per ton of CO_2-equivalent in the next two decades. By the time MANTA enters service, new advancements in production technology will allow for better efficiency and reduced carbon footprint along the fuel production chain and operational phase, hence further reducing the costs.

5.3. Sustainability

The global aviation industry accounts for around 2% of all human-induced carbon emissions [Gro20]. To meet the ambitious goal of reaching carbon neutrality by 2050, the air transport industry is adapting sustainable initiatives at all levels. Aerodynamic changes to design fuel-efficient airframes, efficient engine design, use of lighter materials, innovative production processes, and use of alternative fuels are some ways the industry is trying to achieve further operational efficiency. Hydrogen is gaining serious traction as an alternative fuel source. The use of hydrogen fuel cells eliminates CO_2, CO, NO_x, SO_x and the majority of soot emissions. Water vapor is

however still emitted hence contributing to the rising greenhouse gases level in the atmosphere.[JJ20] estimates that hydrogen combustion could reduce climate impact in-flight by 50-75%, and with fuel-cell technology by 75-90%. As mentioned earlier, compared to kerosene, hydrogen has a higher energy density, however, its higher volume requires larger tanks onboard the aircraft. In contrast to conventional Tube-and Wing (TAW) configuration, a BWB configuration offers more design flexibility to incorporate the large storage tanks required for the hydrogen fuel as well as to incorporate the fuel cell system. Alternative aircraft designs have also been studied over the years in an effort to reduce the climate impact. BWB configuration offers a higher aerodynamic efficiency by integrating the propulsion system, wings, and the body into a lifting body configuration hence reducing noise emission and fuel burn when compared to the classic TAW configuration [Dso12]. Hence it can be considered more environmentally sustainable due to the performance advantages. MANTA is designed to be a BWB configuration and has a lift-to-drag ratio of 24.7. This high ratio implies an improved overall fuel efficiency. Depleting resources, rising global temperatures and growing societal awareness for climate change has increased the importance of environmental sustainability which leads to increased regulatory measures being imposed on flights. Efficient aircraft designs that bring about a reduction in fuel burn and choice of sustainable aviation fuels result in minimized emission pro passenger and hence a greater acceptance of such novel technologies. MANTA is designed while taking these challenges and the sustainability goals into consideration.

6. Feasibility and Conclusions

The challenge of designing a modern hydrogen-powered aircraft is achieved through the combination of innovative strategies and modern technologies. The use of a BWB design has the advantages of improved aerodynamic characteristics as seen in section 3.3 and the use of internal volume for the storage of the liquid hydrogen tanks. The limitations of a BWB design such as the lack of windows and the evacuation in case of emergency were effectively overcome in MANTA as described in section 3.2. The cabin of MANTA provides the passengers with all the comfort expected from a modern first-class aircraft. The use of recycled material on the cabin inside panels also contributes to the green innovation of MANTA. Looking at the operational side, the estimated development and operational costs were derived while taking into consideration all the relevant parameters and new technologies used in the design. The obtained costs provide an insight into the feasibility of the novel concept. The main focus of the design was the energy generation required to power the cabin electrical components and mainly the propulsion system by a PEMFC. The drive train was explained in great detail to show the feasibility of hydrogen powered aircraft and to outline a possible carbon-free future for aviation.

Bibliography

[acc11] ACCU:RATE - INSTITUTE FOR CROWD SIMULATION. *crowd:it* [online]. 2021-02-11 [visited on 2021-06-08]. Available from: https://www.accu-rate.de/de/software-crowd-it-de/.

[Age20] AGENCY, European Aviation Safety. *Certification Specifications and Acceptable Means of Compliance for Large Aeroplanes*. 2020.

[Air17] AIRBUS, SAS. Global Market Forecast: Growing Horizons 2017/2036. 2017, pp. 1–38.

[Ald18] ALDERLIESTEN, R. *Introduction to Aerospace Structures and Materials*. Delft University of Technology, 2018.

[AWK19] ANDERSON, Kevin; John WERITZ; John Gilbert KAUFMAN (eds.). 2195. In: *Properties and selection of aluminum alloys*. Ohio: ASM International, 2019, p. 316. ASM Handbook. ISBN 978-1-62708-210-5. Available from DOI: 10.31399/asm.hb.v02b.a0006608.

[AB20] ANDREAS GOBBIN, Raman Khosravi; Andreas BARDENHAGEN. Emergency evacuation simulation of commercial aircraft. 2020. Available also from: https://doi.org/10.1007/s42452-021-04295-z.

[Bal21] BALLARD POWER SYSTEMS. *Heavy Duty Modules - Fuel Cell Power Products* [online]. 2021 [visited on 2021-04-30]. Available from: https://www.ballard.com/fuel-cell-solutions/fuel-cell-power-products/motive-modules.

[Bar+87] BARNOLA, Jean-Marc; DYSN RAYNAUD, et al. Vostok ice core provides 160,000-year record of atmospheric CO 2. *Nature*. 1987, vol. 329, no. 6138, pp. 408–414.

[bVS07] BJELDE, Brian; Max VOZOFF; Gwynne SHOTWELL. The Falcon 1 Launch Vehicle: Demonstration Flgihts, Status, Manifest, and Upgrade Path [online]. 2007 [visited on 2021-07-02]. Available from: https://digitalcommons.usu.edu/cgi/viewcontent.cgi?referer=&httpsredir=1&article=1456&context=smallsat.

[BM10] BLUNIER, Benjamin; Abdellatif MIRAOUI. Proton Exchange Membrane Fuel Cell Air Management in Automotive Applications. *Journal of Fuel Cell Science and Technology*. 2010, vol. 7, no. 4. ISSN 1550-624X. Available from DOI: 10.1115/1.4000627.

[Boe16] BOEING, Commercial Airplanes. Current Market Outlook 2016-2035. 2016, pp. 4–47.

[BD15] BRADLEY, Marty K.; Christopher K. DRONEY. *Subsonic Ultra Green Aircraft Research: Phase 2: Volume 2: Hybrid Electric Design Exploration* [online]. 2015 [visited on 2021-06-29]. Available from: https://ntrs.nasa.gov/citations/20150017039.

[Bra12] BRANDAU, Nils. *Analyse zur Zellinternen Befeuchtung eines Polymerelektrolytmembran Brennstoffzellenstapels*. Braunschweig: Fakultät Maschinenbau, 2012. [Dissertation]. Technische Universität Carolo-Wilhelmina zu Braunschweig.

[Bre91] BREWER, G.Daniel. *Hydrogen Aircraft Technology*. 1st ed. Bosa Roca: CRC Press, 1991. ISBN 9781351439787. Available also from: https://ebookcentral.proquest.com/lib/gbv/detail.action?docID=5211874.

[Car18] CARDELLA, Umberto Federico. *Large-scale hydrogen liquefaction under the aspect of economic viability* [online]. München: Fakultät Maschinenwesen, 2018 [visited on 2021-07-05]. Available from: https://mediatum.ub.tum.de/doc/1442078/1442078.pdf. [Dissertation]. Technische Universität München.

[CR06] CASEY, M. V.; C. J. ROBINSON. *A guide to turbocharger compressor characteristics*. 2006.

[CF 17] CF AUTOMATION PARTS GMBH & CO. KG. *Zyklonabscheider JK Pneumatik* [online]. Koblenz, 2017 [visited on 2021-04-28]. Available from: https://www.parkerstore-koblenz.com/produkte/aufbereitungstechnik/wasserabscheider/.

[CW97] CHANG, Yu-Juei; Chi-Chuan WANG. A generalized heat transfer correlation for louver fin geometry. *International Journal of Heat and Mass Transfer*. 1997, vol. 40, no. 3, pp. 533–544. ISSN 0017-9310. Available from DOI: 10.1016/0017-9310(96)00116-0.

[Cha+18] CHANG, Yafei; Yanzhou QIN, et al. Humidification strategy for polymer electrolyte membrane fuel cells – A review. *Applied Energy*. 2018, vol. 230, pp. 643–662. ISSN 03062619. Available from DOI: 10.1016/j.apenergy.2018.08.125.

[CP05] CHEN, Dongmei; Huei PENG. A Thermodynamic Model of Membrane Humidifiers for PEMFC Humidification Control. *Journal of Dynamic Systems, Measurement, and Control*. 2005, vol. 127, no. 3, pp. 424–432. ISSN 0022-0434. Available from DOI: 10.1115/1.1978910.

[Cho21] CHOOSE PARIS REGION. *H2 Hub Airport* [online]. 2021 [visited on 2021-07-01]. Available from: https://www.chooseparisregion.org/calls-for-applications/h2-hub-airport.

[Cli] CLIMATE.NASA.GOV. *The relentless rise of carbon dioxide* [online] [visited on 2021-07-13]. Available from: https://climate.nasa.gov/climate_resources/24/graphic-the-relentless-rise-of-carbon-dioxide/.

[Con17] CONSTELLIUM. Airware® 2195-T84 PLATE [online]. 2017 [visited on 2021-05-03]. Available from: www.constellium.com/sites/default/files/markets/airware_2195_t84_plate.pdf.

[COR03] CORDIS. *Liquid Hydrogen Fuelled Aircraft – System Analysis: Final technical report: Cryoplane* [online]. 2003 [visited on 2021-05-16]. Available from: https://cordis.europa.eu/project/id/G4RD-CT-2000-00192/de.

[Cou20] COUNCIL, Hydrogen. *Path to Hydrogen Competitiveness - A cost perspective* [online]. 2020 [visited on 2021-06-04].

[Cro19] CRONKLETON, Emily. *What is the average walking speed of an adult* [online]. 2019 [visited on 2021-07-06]. Available from: https://www.healthline.com/health/exercise-fitness/average-walking-speed.

[Dso12] D'SOUZA, S. I. An analysis of the developments in blended wing body aircraft for sustainable aviation. 2012.

[DJ19] DAKKA, Sam Dr; Oliver JOHNSON. Aerodynamic Design and Exploration of a Blended Wing Body Aircraft at Subsonic Speed. *IJAAA*. 2019, vol. 6, pp. 7–8. Available from DOI: 10.15394/ijaaa.2019.1411.

[Dan+19] DANIEL SILBERHORN; GEORGI ATANASOV, et al. Assessment of Hydrogen Fuel Tank Integration at Aircraft Level. In: 2019. Available also from: https://www.researchgate.net/publication/336641820_Assessment_of_Hydrogen_Fuel_Tank_Integration_at_Aircraft_Level.

[DLR21] DLR. *NASA/DLR Aeronautics Design Challenge 2021* [online]. 2021 [visited on 2021-05-10]. Available from: https://www.dlr.de/content/en/articles/education/nasa-dlr-design-challenge.html.

[Don00] DONACHIE, Matthew J. *Titanium: A technical guide*. 2nd ed. Materials Park, OH: ASM International, 2000. ISBN 9781615030620.

[DG11] DORBATH, Felix; Ulf GAIDA. *Large Civil Jet Transport (MTOM > 40t) - Statistical Mass Estimation*. 2011. Available also from: https://elib.dlr.de/81599/.

[Fel16] FELDER, James L. *Timeline of Machine Power With Application to Aircraft Class: NASA Electric Propulsion System Studies* [online]. [online], 2016 [visited on 2021-04-28]. Available from: https://ntrs.nasa.gov/api/citations/20160009274/downloads/20160009274.pdf.

[FB09] FELDER, James L. ; Kimm Hyun Dae; Gerald V. BROWN. Turboelectric Distributed Propulsion Engine Cycle Analysis for Hybrid-Wing-Body Aircraft. *AIAA*. 2009. Available from DOI: 10.2514/6.2009-1132.

[Fer+18] FERNANDES, M. D.; S. T. de P. ANDRADE, et al. SOFC-APU systems for aircraft: A review. *International Journal of Hydrogen Energy*. 2018, vol. 43, no. 33, pp. 16311–16333. ISSN 0360-3199. Available from DOI: 10.1016/j.ijhydene.2018.07.004.

[Fra15] FRAUNHOFER INSTITUTE FOR INTEGRATED SYSTEMS AND DEVICE TECHNOLOGY IISB. *HIgh Power SiC DC/DC Converters* [online]. Erlangen, 2015 [visited on 2021-04-25]. Available from: https://www.iisb.fraunhofer.de/content/dam/iisb2014/en/Documents/Research-Areas/vehicle_electronics/Publications/DCDC_Converters/PDB_HighPowerSiC.pdf.

[Gar16] GARDINER, Ginger. *Recycled carbon fiber proves its potential for aircraft interiors* [online]. 2016 [visited on 2021-06-06]. Available from: https://www.compositesworld.com/articles/recycled-carbon-fiber-proves-its-potential-for-aircraft-interiors.

[Gie21] GIERENS, Klaus. Theory of Contrail Formation for Fuel Cells. *Aerospace*. 2021, vol. 8, no. 6, p. 164. Available from DOI: 10.3390/aerospace8060164.

[Gre+21] GREWE, Volker; Arvind Gangoli RAO, et al. Evaluating the climate impact of aviation emission scenarios towards the Paris agreement including COVID-19 effects. *Nature Communications*. 2021, vol. 12, no. 1, pp. 1–10.

[Gro20] GROUP, Air Transport Action. *Facts and Figures* [online]. September 2020 [visited on 2021-07-07]. Available from: https://www.atag.org/facts-figures.html.

[Gud13] GUDMUNDSSON, S. *General Aviation Aircraft Design: Application Methods and Procedures*. Butterworth Heinemann, 2013.

[Guo+13] GUO, Ai; Weirong CHEN, et al. Air flow control based on optimal oxygen excess ratio in fuel cells for vehicles. *Journal of Modern Transportation*. 2013, vol. 21, no. 2, pp. 79–85. ISSN 2095-087X. Available from DOI: 10.1007/s40534-013-0009-8.

[HHS06] HAGLIND, F.; A. HASSELROT; R. SINGH. Potential of reducing the environmental impact of aviation by using hydrogen Part I: Background, prospects and challenges. *The Aeronautical Journal (1968)*. 2006, vol. 110, no. 1110, pp. 533–540. Available from DOI: 10.1017/S000192400000141X.

[Hep21a] HEPPERLE, Martin. *MH 61 10.2% (mh61-il)* [online]. 2021 [visited on 2021-07-16]. Available from: http://airfoiltools.com/airfoil/details?airfoil=mh61-il.

[Hep21b] HEPPERLE, Martin. *MH 91 14.98% (mh91-il)* [online]. 2021 [visited on 2021-07-05]. Available from: http://airfoiltools.com/airfoil/details?airfoil=mh91-il.

[HW17] HESHMAT, Hooshang; James F. WALTON. A Bladeless Turbocompressor Concept: Shear Driven Gas Compression With Deformable Structures: Part 1 — Experimental Proof of Concept. In: *Proceedings of the ASME Power Conference joint with ICOPE-17 - 2017*. New York, N.Y.: The American Society of Mechanical Engineers, 2017. ISBN 978-0-7918-5760-1. Available from DOI: 10.1115/POWER-ICOPE2017-3374.

[Hes01] HESSELGREAVES, John E. *Compact heat exchangers: Selection, design, and operation*. Amsterdam and New York: Pergamon, 2001. ISBN 0080529542.

[Hon15] HONGFANG S Guanping G, etc. Recycling of carbon fibers from carbon fiber reinforced polymer using electrochemical method. 2015. Available also from: https://www.researchgate.net/publication/281198090_Recycling_of_carbon_fibers_from_carbon_fiber_reinforced_polymer_using_electrochemical_method.

[Hyg17] HYGROMATIK GMBH. *Adiabate Nieder- und Hochdrucksysteme LPS und HPS* [online]. 2017 [visited on 2021-04-28]. Available from: https://www.hygromatik.com/de/adiabate-nieder-und-hochdrucksysteme-lps-und-hps.

[JM13] J WINZEN, F Albers; C MARGGRAF-MICHEEL. The influence of coloured light in the aircraft cabin on passenger thermal comfort. 2013. Available also from: https://doi.org/10.1177/1477153513484028d.

[JJ20] JU, Clean Sky 2; FCH 2 JU. Hydrogen-powered aviation: A fact based study of hydrogen technology, economics and climate impact by 2050 [online]. May 2020 [visited on 2021-06-04].

[Kab21] KABZA, Alexander. *Fuel Cell Formulary* [online]. 2021 [visited on 2021-03-02]. Available from: http://www.pemfc.de/FCF_A4.pdf.

[KP15] KAISER, J.; PROF. DR. BURKHARD HEINE. Tieftemperaturverhalten rostfreier Edelstähle. *WOTech GbR* [online]. 2015 [visited on 2021-04-05]. Available from DOI: 10.7395/2015/Heine3.

[Kel+21] KELLERMANN, Hagen; Michael LÜDEMANN, et al. Design and Optimization of Ram Air–Based Thermal Management Systems for Hybrid-Electric Aircraft. *Aerospace*. 2021, vol. 8, no. 1, p. 3. Available from DOI: 10.3390/aerospace8010003.

[KCK15] KIM, Bosung; Dowon CHA; Yongchan KIM. The effects of air stoichiometry and air excess ratio on the transient response of a PEMFC under load change conditions. *Applied Energy*. 2015, vol. 138, pp. 143–149. ISSN 03062619. Available from DOI: 10.1016/j.apenergy.2014.10.046.

[KS15] KOZEK, Martin; Alexander SCHIRRER. *Modeling and Control for a Blended Wing Body Aircraft*. Springer, 2015. ISBN 978-3-319-10791-2.

[Lab99] LABITZKE, Karin G. *Die Stratosphäre: Phänomene, Geschichte, Relevanz*. Berlin: Springer, 1999. ISBN 3540650008.

[Lan21] LANGLEY RESEARCH CENTER. *openVSP NASA Open Source Parametric Geometry*. 2021. Version 3.24.0. Available also from: http://openvsp.org.

[Lar+18] LARIBI, Slimane; Khaled MAMMAR, et al. Air supply temperature impact on PEMFC impedance. *Journal of Energy Storage*. 2018, vol. 17, pp. 327–335. ISSN 2352152X. Available from DOI: 10.1016/j.est.2018.03.020.

[Li+21] LI, Yan; Yonglei ZHANG, et al. A 500kW Forced-air-cooled Silicon Carbide (SiC) 3-Phase DC/AC Converter with a Power Density of 1.246MW/m3 and Efficiency >98.5%. *IEEE Transactions on Industry Applications*. 2021, p. 1. ISSN 1939-9367. Available from DOI: 10.1109/TIA.2021.3087546.

[Lin13] LINDE GMBH. *Tankanlagen zur Versorgung mit verflüssigten Gasen: LIN, LOX, LAR, CO2* [online]. 2013 [visited on 2021-04-05]. Available from: https://www.linde-gas.de/de/images/Tankanlagen_Fluessiggase_tcm565-71606.pdf.

[Lin+20] LINKE, Florian; Kaushik RADHAKRISHNAN, et al. GLOWOPT-A new approach towards global-warming-optimized aircraft design. 2020.

[Löh11] LÖHN, Helmut. *Leistungsvergleich von NT- und HT-PEM-Brennstoffzellen: Experimentelle Untersuchungen, Modellierung und numerische Simulation*. Neue Ausg. Saarbrücken: Suedwestdeutscher Verlag fuer Hochschulschriften, 2011. ISBN 3838124146.

[Lüd+11] LÜDDERS, Hauke Peer; Jan GRYMLAS, et al. A Methodology for Rapid Evaluation and Sizing of Fuel Cell System Architectures for Commercial Aircraft. *SAE International Journal of Aerospace*. 2011, vol. 4, no. 2, pp. 1084–1096. ISSN 1946-3901. Available from DOI: 10.4271/2011-01-2646.

[LST13] LÜDDERS, Hauke Peer; Hendrik STRUMMEL; Frank THIELECKE. Model-based development of multifunctional fuel cell systems for More-Electric-Aircraft. *CEAS Aeronautical Journal*. 2013, vol. 4, no. 2, pp. 151–174. ISSN 1869-5582. Available from DOI: 10.1007/s13272-013-0062-3.

[MJE04] MARK D. GUYNN; JOSHUA E. FREH; ERIK D. OLSON. *Evaluation of a Hydrogen Fuel Cell Powered Blended-Wing-Body Aircraft Concept for Reduced Noise and Emissions* [online]. 2004 [visited on 2021-06-16]. Available from: https://ntrs.nasa.gov/api/citations/20040033924/downloads/20040033924.pdf.

[Moh21] MOHAWK INNOVATIVE TECHNOLOGY. *Oil-Free Turbomachinery* [online]. 2021 [visited on 2021-06-30]. Available from: https://mohawkinnovative.com/oil-free-turbomachinery/.

[MS10] MS. KAREN M.B. TAMINGER; STEPHEN J. HALES. Aerospace Applications of Aluminum-Lithium Alloy Thick Plate. In: 2010. Available also from: https://www.researchgate.net/publication/267900529_Aerospace_Applications_of_Aluminum-Lithium_Alloy_Thick_Plate.

[Mur38] MURRAY, William MacGregor. Heat Dissipation Through an Annular Disk or Fin of Uniform Thickness. *Journal of Applied Mechanics*. 1938, vol. 5, no. 2, A78–A80. ISSN 0021-8936. Available from DOI: 10.1115/1.4008851.

[Nat05] NATIONAL AERONAUTICS AND SPACE ADMINISTRATION. *Super Lightweight External Tank* [online]. Huntsville, 2005 [visited on 2021-05-05]. Available from: https://www.nasa.gov/sites/default/files/113020main_shuttle_lightweight.pdf.

[Nat77] NATIONAL BUREAU OF STANDARDS. *LNG Materials and Fluids*. 1977.

[Niž20] NIŽETIĆ, Sandro. Impact of coronavirus (COVID-19) pandemic on air transport mobility, energy, and environment: A case study. *International Journal of Energy Research*. 2020, vol. 44, no. 13, pp. 10953–10961.

[NDN09] NOJOUMI, H.; I. DINCER; G. NATERER. Greenhouse gas emissions assessment of hydrogen and kerosene-fueled aircraft propulsion. *International Journal of Hydrogen Energy*. 2009, vol. 34, no. 3, pp. 1363–1369. ISSN 0360-3199. Available from DOI: 10.1016/j.ijhydene.2008.11.017.

[Oeh09] OEHLKE, Martin. *Masseabschätzung eines Wasserstoff Außentanks für ein Turboprop Verkehrsflugzeug*. Hamburg, 2009. Available also from: https://www.fzt.haw-hamburg.de/pers/Scholz/arbeiten/TextOehlkeMasse.pdf. [Project]. Hamburg University of Applied Sciences.

[OM14] ORDOUKHANIAN, Edwin; Azad M. MADNI. Blended Wing Body Architecting and Design: Current Status and Future Prospects. *Procedia Computer Science*. 2014, vol. 28, pp. 619–625. ISSN 1877-0509. Available from DOI: https://doi.org/10.1016/j.procs.2014.03.075. 2014 Conference on Systems Engineering Research.

[Pim11] PIMENTA S, Pinho ST. Recycling carbon fibre reinforced polymers for structural applications: Technology review and market outlook. 2011, vol. 31, pp. 378–392. ISSN 0956-053X. Available also from: https://www.sciencedirect.com/science/article/pii/S0956053X10004976.

[Pow21] POWERCELLUTION. *P Stack* [online]. 2021 [visited on 2021-06-22]. Available from: https://powercellution.com/p-stack.

[PGW14] PRASAD, N. Eswara; Amol A. GOKHALE; Russell J. H. WANHILL (eds.). *Aluminum-lithium alloys: Processing, properties, and applications*. Amsterdam: BH Butterworth-Heinemann/Elsevier, 2014. ISBN 9780124016989. Available also from: http://www.loc.gov/catdir/enhancements/fy1606/2014469188-d.html.

[R P+91] R. P. REED; P. T. PURTSCHER, et al. *Aluminum Alloys for ALS Cryogenic Tanks: Comparative Measurements of Cryogenic Mechanical Properties of Al-Li Alloys and Alloy 2219*. 1991. Available also from: https://www.researchgate.net/publication/235071483_Aluminum_Alloys_for_ALS_Cryogenic_Tanks_Comparative_Measurements_of_Cryogenic_Mechanical_Properties_of_Al-Li_Alloys_and_Alloy_2219.

[Raj+13] RAJA SEKARAN, Paulas; Amir S. GOHARDANI, et al. Liquid hydrogen tank considerations for turboelectric distributed propulsion. *Aircraft Engineering and Aerospace Technology*. 2013, vol. 86, no. 1, pp. 67–75. ISSN 0002-2667. Available from DOI: 10.1108/AEAT-12-2011-0195.

[Ran14] RANA, Radhakanta. Low-Density Steels. *JOM*. 2014, vol. 66, no. 9, pp. 1730–1733. ISSN 1543-1851. Available from DOI: 10.1007/s11837-014-1137-2.

[Ray18] RAYMER, Daniel P. *Aircraft design: A conceptual approach*. Sixth edition. Reston, VA: American Institute of Aeronautics and Astronautics Inc, 2018. AIAA education series. ISBN 9781624104909.

[RWH14] ROSSOW, C.C.; K. WOLF; P. HORST. *Handbuch der Luftfahrzeugtechnik*. Carl Hanser Verlag GmbH & Company KG, 2014. ISBN 9783446436046. Available also from: https://books.google.de/books?id=xauQAgAAQBAJ.

[Sch15] SCHALBE, Dr.-Ing. Daniel. Modellbasierte Entwicklung von Energiemanagement-Methoden für Flugzeug-Energiesysteme. 2015. ISBN 9 978-3-18-346220-9. Available also from: https://nbn-resolving.org/urn:nbn:de:bsz:14-qucosa-217893.

[SQ06] SIOURIS, S; N QIN. Study of the effects of wing sweep on the aerodynamic performance of a blended wing body aircraft. *Aerodynamics and Thermofluids Group, Department of Mechanical Engineering, University of Sheffield, Sheffield, UK*. 2006, pp. 1–9. Available from DOI: 10.1243/09544100JAERO93.

[SMB98] SMITH, Douglas M.; Alok MASKARA; Ulrich BOES. Aerogel-based thermal insulation. *Journal of Non-Crystalline Solids*. 1998, vol. 225, pp. 254–259. ISSN 00223093. Available from DOI: 10.1016/S0022-3093(98)00125-2.

[Spa07] SPACE EXPLORATION TECHNOLOGIES. *Falcon 9 overview* [online]. 2007 [visited on 2021-04-02]. Available from: https://web.archive.org/web/20070210095458/http://spacex.com/falcon9.php.

[Spe13] SPENCER, K.M. Investigation of Potential Fuel Cell Use in Aircraft [online]. 2013 [visited on 2021-06-21]. Available from: https://www.ida.org/-/media/feature/publications/i/in/investigation-of-potential-fuel-cell-use-in-aircraft/d-5043.ashx.

[Sta20] STATISTA. *Age distribution of air passengers in the United Kingdom (UK) in 2019* [online]. 2020 [visited on 2021-07-06]. Available from: https://www.statista.com/statistics/304641/age-distribution-of-air-passengers-by-airport-uk/.

[Tay+20] TAYEBI, S. Milad; Wei XU, et al. A Single-Stage Isolated Resonant SiC DC/AC Inverter for Efficient High-Power Applications. In: *2020 IEEE Applied Power Electronics Conference and Exposition (APEC)*. IEEE, 2020. ISBN 9781728148298. Available from DOI: 10.1109/apec39645.2020.9124343.

[Ver16] VEREIN DEUTSCHER INGENIEURE E.V. / VERBAND DER ELEKTROTECHNIK ELEKTRONIK INFORMATIONSTECHNIK E. V. *Measurement of gas humidity - Characteristics and symbols*. Berlin: Beuth, 2016. No. 3514 Blatt 1.

[Ver09] VERSTRAETE, Dries. *The Potential of Liquid Hydrogen for long range aircraft propulsion*. Cranfield University, 2009. Available also from: https://dspace.lib.cranfield.ac.uk/bitstream/1826/4089/1/D_Verstraete_Thesis_2009.pdf. [Dissertation].

[Ver13] VERSTRAETE, Dries. Long range transport aircraft using hydrogen fuel. *International Journal of Hydrogen Energy*. 2013, vol. 38, no. 34, pp. 14824–14831. ISSN 0360-3199. Available from DOI: 10.1016/j.ijhydene.2013.09.021.

[Whi+19] WHISTON, Michael M.; Inês L. AZEVEDO, et al. Expert assessments of the cost and expected future performance of proton exchange membrane fuel cells for vehicles. *Proceedings of the National Academy of Sciences of the United States of America*. 2019, vol. 116, no. 11, pp. 4899–4904. Available from DOI: 10.1073/pnas.1804221116.

[Wu+12] WU, Wenhua; Dehua CHEN, et al. A New Efficient Control Method for Blended Wing Body. *International Journal of Modern Physics: Conference Series*. 2012, vol. 19, pp. 396–405.

[Zha+14] ZHAO, Dongdong; Benjamin BLUNIER, et al. Control of an Ultrahigh-Speed Centrifugal Compressor for the Air Management of Fuel Cell Systems. *IEEE Transactions on Industry Applications*. 2014, vol. 50, no. 3, pp. 2225–2234. ISSN 1939-9367. Available from DOI: 10.1109/TIA.2013.2282838.

[Zhe19] ZHENLI C. H. E. N., et al. Assessment on critical technologies for conceptual design of blended-wing-body civil aircraft. *TChinese Journal of Aeronautics, 32(8)*. 2019, pp. 1797–1827.

Appendices

A. Cabin Dimensions

Table A.1.: BC Class Cabin Dimensions

Description	Value	Unit
Cabin Diameter	3.05	m
Cabin Height	2.20	m
Cabin Length	6.14	m
Floor Width	3.43	m
Passenger	16	-
Crew	1	-
Number of Aisle	1	-
Aisle Width	0.508	m
Aisle Height	2.2	m
Seat Pitch	1.43	m
Seat Width	0.61	m
Seat Height	1.19	m
Arm Rest Height	0.65	m
Wall Thickness	0.09	m

Table A.2.: EC Class Cabin Dimensions

Description	Value	Unit
Cabin Diameter	6.196	m
Cabin Height	2.20	m
Floor Width	6.096	m
Cabin Length	16.19	m
Passenger	134	-
Crew	3	-
Number of Aisle	2	-
Aisle Width	0.508	m
Aisle Height	2.2	m
Seat Pitch	0.889	m
Seat Width	0.508	m
Seat Height	1.19	m
Arm Rest Height	0.65	m
Wall Thickness	0.09	m

B. Passenger Simulation Parameters

Table B.3.: Passenger Load used in the simulation [Sta20]

Profile	Percentage[%]	150 PAX	Female	Male
Age 20-29	20	30	14	16
Age 30-39	24	36	17	16
Age 40-49	21	32	15	16
Age 50-59	17	25	12	13
Age 60-69	10	15	7	8
Age 70-79	5	8	4	4
Age 80-89	3	5	3	2

* 48% passengers are female

Table B.4.: Passenger walking speed raw date [Cro19]

Profile	Mean speed[m/s]	Standard deviation[m/s]	Maximum speed [m/s]	Minimum speed [m/s]
20-29 Male	1.36	0.196	1.752	0.968
20-29 Female	1.34	0.211	1.762	0.918
30-39 Male	1.43	0.205	1.84	1.02
30-39 Female	1.34	0.213	1.766	0.914
40-49 Male	1.43	0.229	1.888	0.972
40-49 Female	1.39	0.151	1.692	1.088
50-59 Male	1.43	0.164	1.758	1.102
50-59 Female	1.31	0.158	1.626	0.994
60-69 Male	1.34	0.094	1.528	1.152
60-69 Female	1.24	0.127	1.494	0.986
70-79 Male	1.26	0.153	1.566	0.954
70-79 Female	1.13	0.175	1.48	0.78
80-89 Male	0.97	0.1	1.17	0.77
80-89 Female	0.94	0.1	1.14	0.74

Table B.5.: Passenger walking speed calculated date in simulation

Mean speed[m/s]	Standard deviation[m/s]	Maximum speed [m/s]	Minimum speed [m/s]
0.937	0.178	1.187	0.686

C. Geometric Parameters

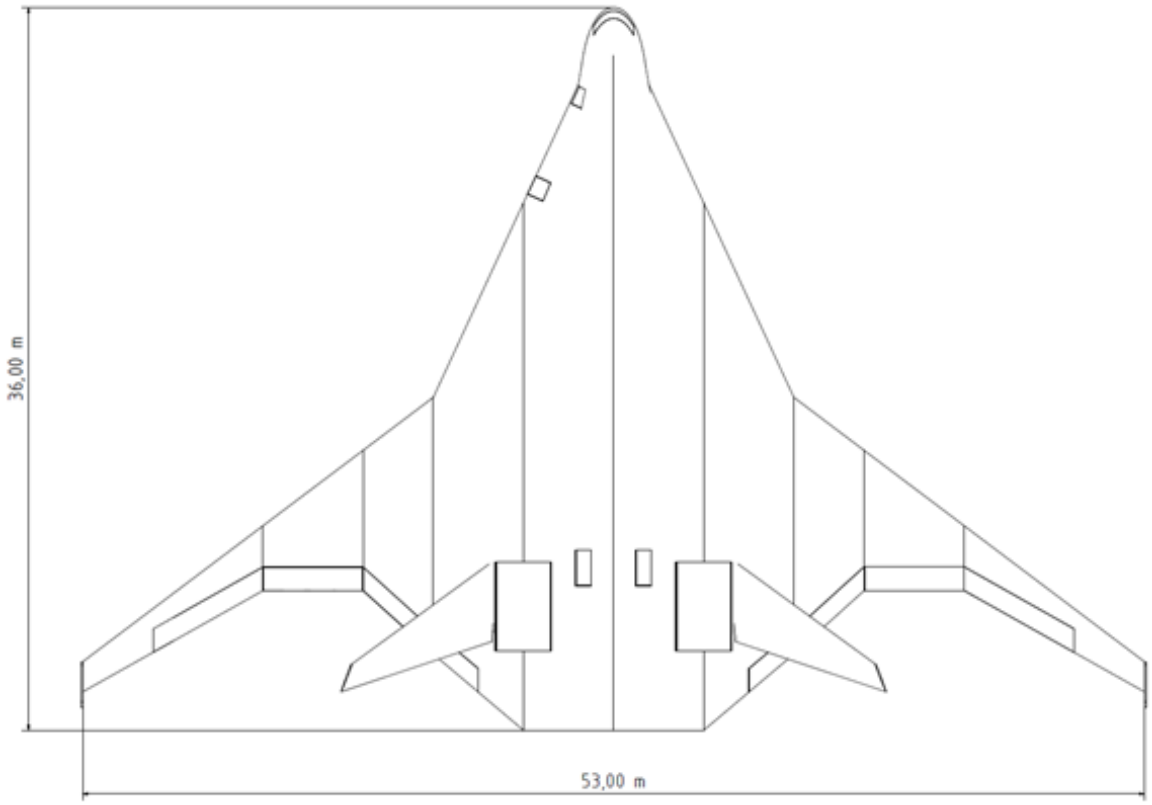

Figure C.1.: Top View

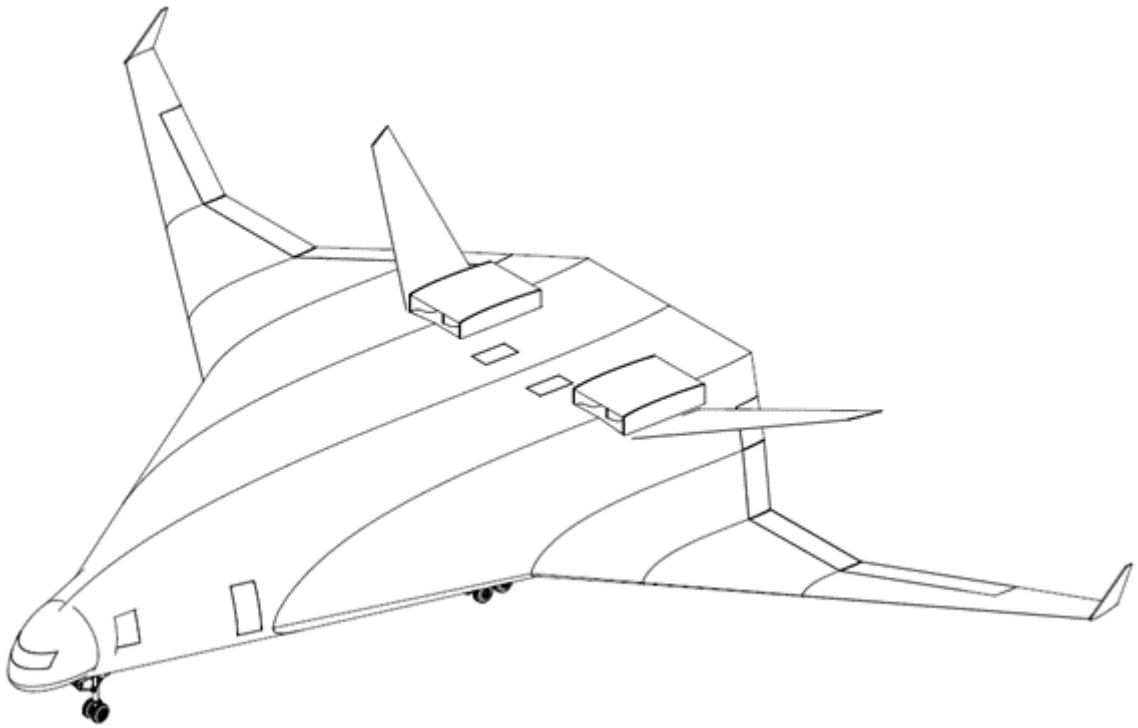

Figure C.2.: Isometric View

D. Miscellaneous

Table D.6.: Initial sizing comparison between flight levels and LOX tank integration

		3000m + LOX		**6000m + LOX**		**6000m no LOX**	
	Unit	Mission 1	Mission 2	Mission 1	Mission 2	Mission 1	Mission 2
LH2 Volume	m^3	38.04	84.78	39.00	88.00	40.00	76.00
LH2 Tank Mass empty	kg	1506.50	3111.10	2012.50	4085.20	2052.00	3565.00
LH2 Tank Mass full	kg	3451.8	7522.40	4414.90	9538.70	4522.00	8301.00
LOX Volume	m^3	3.78	8.55	4.26	9.67	0.00	0.00
LOX Tank Mass empty	kg	1081.40	2407.90	1197.00	2735.40	0.00	0.00
LOX Tank Mass full	kg	4097.40	9236.70	4598.10	10 456.00	0.00	0.00
Mass Fuel Cell Stack	kg	8170.00	8170.00	8084.00	8084.00	10 752.00	10 752.00
Mass Compressor	kg	1942.30	1942.30	3027.40	3027.40	4711.70	4711.70
Mass Heat Exchanger	kg	9326.20	9326.20	11 066.00	11 066.00	14 505.00	14 505.00
Mass H2O System	kg	2998.90	2998.90	3548.00	3548.00	5512.20	5512.20
Mass Total	kg	29 986.60	39 196.50	34 738.40	45 720.10	**40 002.90**	**43 781.90**
Volume Fuel Cell Stack	m^3	7.07	7.07	7.00	7.00	9.52	9.52
Volume Heat Exchanger	m^3	8.91	8.91	10.57	10.57	13.85	13.85
Volume Humidifier	m^3	4.77	4.77	5.66	5.66	8.78	8.78
Volume Waterseparator	m^3	6.47	6.47	6.47	6.47	6.47	6.47
Mission Distance (apprx.)	m	969 400	2 369 400	969 400	2 369 400	969 400	2 369 400
Flighttime (apprx.)	s	4215	10 902	4977	11 297	4299	14 329
Max. Required Power	MW	25.18	25.18	27.48	27.48	38.48	38.48
Power Density	kW/L	3.11	3.11	3.14	3.14	2.63	2.63
Non-recurring Costs (Fuel Cell System)	$	1 158 463	1 158 464	1 263 896	1 263 896	1 770 080	1 770 080
Non-recurring Costs (Fuel Cell System)	€	949 940	949 940	1 036 395	1 036 395	1 451 466	1 451 466

Table D.7.: Heat Exchanger geometric assumption [CW97]

Parameter	Value	Description
h_{tube}	0.275 m	Tube height
b_{tube}	0.01 m	Tube width
t_{tube}	0.000 32 m	Tube wall thickness
h_{fin}	0.012 m	Fin height
t_{fin}	0.000 075 m	Fin thickness
$\text{pitch}_{\text{fin}}$	0.0015 m	Fin offset
θ	20°	Fin angle
$\text{pitch}_{\text{louver}}$	0.002 25 m	Fin cut offset
l_{louver}	0.0095 m	Fin cut length

Figure D.3.: MANTA Take Off

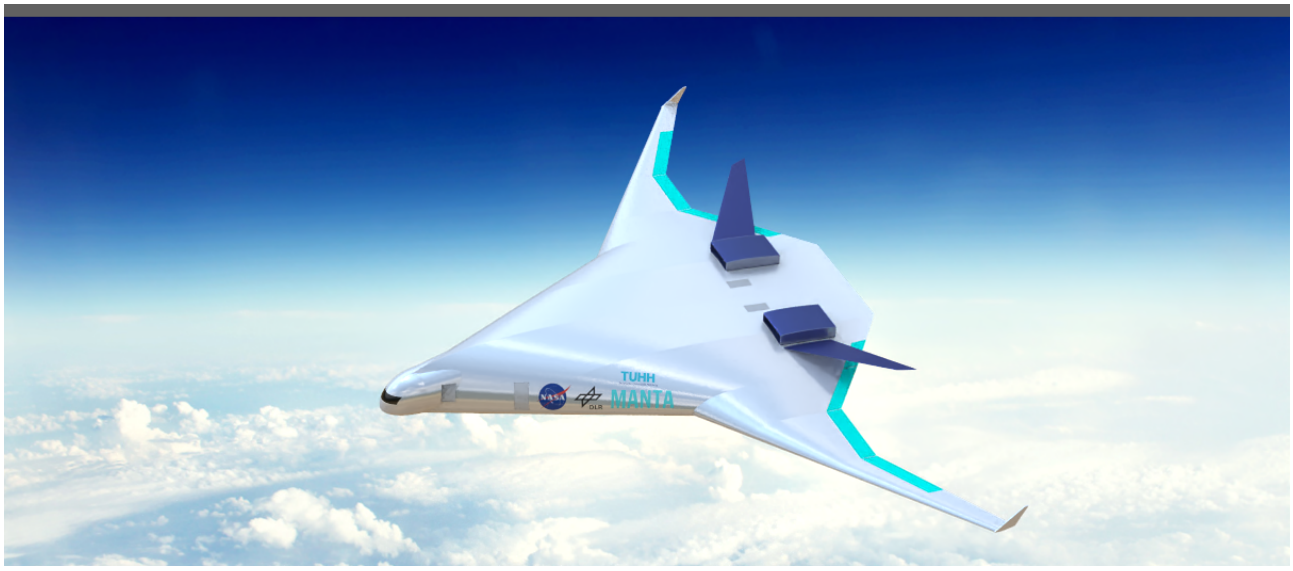

Figure D.4.: MANTA in flight

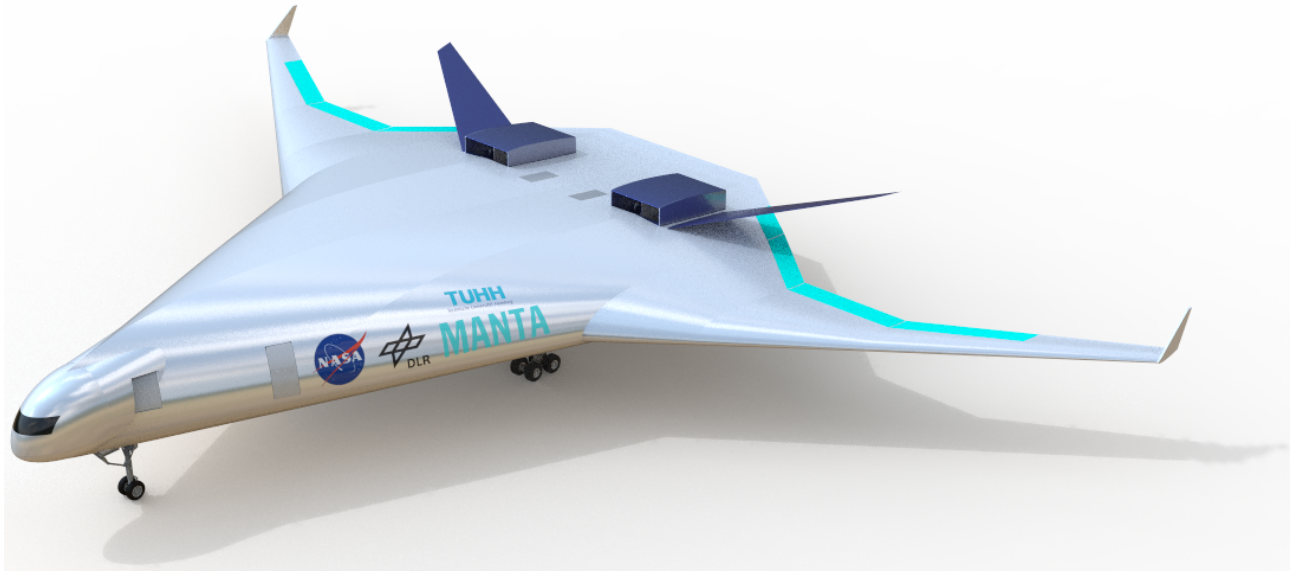

Figure D.5.: MANTA BWB